

Water Resources Research

RESEARCH ARTICLE

10.1029/2020WR027743

Key Points:

- MFR is a large recharge component in semiarid valley aquifers, but MFR components are difficult to quantify and sensitive to climate change
- Age distributions, noble gas thermometry, and fluid/energy transport modeling combined as an approach to distinguish/quantify MFR components
- Noble gas thermometry can help constrain age distributions, but assuming a constant T_r lapse rate may produce improbable recharge elevations because surface MFR can locally suppress water table temperatures in basin-fill aquifers

Supporting Information:

- Supporting Information S1

Correspondence to:

K. H. Markovich,
kmarkovich@intera.com

Citation:






Markovich, K. H., Condon, L. E., Carroll, K. C., Purtschert, R., & McIntosh, J. C. (2021). A mountain-front recharge component characterization approach combining groundwater age distributions, noble gas thermometry, and fluid and energy transport modeling. *Water Resources Research*, 57, e2020WR027743. <https://doi.org/10.1029/2020WR027743>

Received 16 APR 2020

Accepted 20 NOV 2020

© 2020. American Geophysical Union.
All Rights Reserved.

A Mountain-Front Recharge Component Characterization Approach Combining Groundwater Age Distributions, Noble Gas Thermometry, and Fluid and Energy Transport Modeling

Katherine H. Markovich^{1,2} , Laura E. Condon¹ , Kenneth C. Carroll³ ,
Roland Purtschert⁴ , and Jennifer C. McIntosh¹ 

¹Department of Hydrology and Atmospheric Sciences, University of Arizona, Tucson, AZ, USA, ²Now at INTERA Inc., Albuquerque, NM, USA, ³Plant and Environmental Sciences Department, New Mexico State University, Las Cruces, NM, USA, ⁴Climate and Environmental Physics, University of Bern, Bern, Switzerland

Abstract Mountain-front recharge (MFR), or all inflow to a basin-fill aquifer with its source in the mountain block, is an important component of recharge to basin-fill aquifer systems. Distinguishing and quantifying the surface from subsurface components of MFR is necessary for water resource planning and management, particularly as climate change may impact these components in distinct ways. This study tests the hypothesis that MFR components can be distinguished in long-screened, basin-fill production wells by (1) groundwater age and (2) the median elevation of recharge. We developed an MFR characterization approach by combining age distributions in six wells using tritium, krypton-85, argon-39, and radiocarbon, and median recharge elevations from noble gas thermometry combined with numerical experiments to determine recharge temperature lapse rates using flow and energy transport modeling. We found that groundwater age distributions provided valuable information for characterizing the dominant flow system behavior captured by the basin-fill production wells. Tracers indicated the presence of old (i.e., no detectable tritium) water in a well completed in weathered bedrock located close to the mountain front. Two production wells exhibited age distributions of binary mixing between modern and a small fraction of old water, whereas the remaining wells captured predominantly modern flow paths. Noble gas thermometry provided important complementary information to the age distributions; however, assuming constant recharge temperature lapse rates produced improbable recharge elevations. Numerical experiments suggest that surface MFR, if derived from snowmelt, can locally suppress water table temperatures in the basin-fill aquifer, with implications for recharge elevations estimated from noble gas thermometry.

1. Introduction

Mountain-front recharge (MFR), defined as all inflow to a basin-fill aquifer with its source in the mountain block (Markovich et al., 2019), is an important water budget component globally, particularly in arid and semiarid regions (Wilson & Guan, 2004). Shifts in water supply in mountainous systems induced by climate change are likely to alter the timing and magnitude of MFR (Meixner et al., 2016), and demand-side stresses on basin-fill aquifers will likely increase as surface water supplies become less reliable (Taylor et al., 2013). As these stresses intensify, we are challenged to predict future MFR. To do this effectively, we must better quantify the processes controlling MFR and the components of MFR with improved characterization of flow and transport time scales.

Mountain-front recharge components can be divided into three types: (1) surface MFR, or recharge that occurs as infiltration from ephemeral and perennial streams along the mountain front; (2) diffuse mountain-block recharge (MBR), or spatially distributed subsurface inflow from the mountain block to the adjacent basin fill; and (3) focused MBR, or subsurface inflow that occurs along discrete, permeable geologic features such as a fault or beneath streams in the unconsolidated sediment (Markovich et al., 2019; Wilson & Guan, 2004). Distinguishing between these components is necessary as they operate on different spatial and temporal scales, and thus could respond to climate change in profoundly different ways. However, characterizing MFR components is challenging because, first, they often exhibit similar chemical and stable

isotopic signatures and, second there are rarely deep wells located in the mountain block or near the mountain front from which to directly observe MBR.

Groundwater age dating is one way to address both of these challenges. While different MFR components often exhibit similar chemical and isotopic signatures, they may differ substantially in flow path length and flow velocity, which is in turn recorded by the time elapsed since recharge or groundwater age. For example, given the generally longer flow paths and orders of magnitude lower hydraulic conductivities in mountain blocks compared to basin-fill aquifers, diffuse MBR should exhibit significantly older ages than surface MFR. Groundwater age dating using multiple tracers can also be used to address the second challenge. While the availability of deep wells completed in the mountain block or at the mountain front is limited, there is often a relative abundance of deep, long-screened production wells completed in the basin-fill aquifer that can capture a range of flow paths (Visser et al., 2013). An integration of these flow paths yields the age distribution for the production well. MFR components can be interpreted from this distribution using multiple tracers able to date various age intervals. The most commonly applied tracers are those used for dating “modern” groundwater, or water recharged since the 1950s, including chlorofluorocarbons (CFCs), sulfur hexafluoride (SF_6), and tritium-helium ($^3\text{H}/^3\text{He}$) (Schlosser et al., 1988; Solomon & Cook, 2000). Old groundwaters can be dated up to 30 ky using radiocarbon (^{14}C), and up to 1 Ma using chlorine-36 (^{36}Cl), and helium-4 (^4He) (Aggarwal et al., 2013).

More recently, advances in measurement of ultratrace noble gas radioisotopes has paved the way for more common, though not yet routine, applications of krypton-85 (^{85}Kr), argon-39 (^{39}Ar), and, krypton-81 (^{81}Kr) for dating modern, intermediate, and old groundwater ages, respectively (Jiang et al., 2012; Loosli & Purtschert, 2005; Riedmann & Purtschert, 2016; Yokochi, 2016). These tracers are well-suited for groundwater age applications as they are inert, and, in the case of ^{39}Ar and ^{81}Kr , are predominantly cosmogenic (Loosli et al., 2000). In particular, ^{39}Ar , which has a half-life of 269 years, fills an important and longstanding gap between modern age tracers and ^{14}C , making it distinctly valuable for age distribution studies. While dissolved noble gas radioisotopes hold great promise, there are significant challenges that have precluded the widespread adoption of them in groundwater age applications. Namely, their ultralow abundance requires the difficult collection of large volumes of dissolved gas and analytical procedures are both costly and time-consuming. Nevertheless, a handful of studies have included ^{85}Kr and ^{39}Ar in multitracers approaches to rigorously characterize the age distributions of production wells (Åkesson et al., 2015; Corcho Alvarado et al., 2007; Visser et al., 2013). These studies demonstrate the ability of noble gas radioisotopes in multitracers approaches to reduce uncertainty in age distribution modeling and to better distinguish modern from premodern groundwater in samples collected from long-screened production wells.

Given the often-limited number of wells sampled and uncertainty associated with age distribution modeling, additional environmental tracers such as noble gases can provide information that is crucial for characterizing MFR components. In addition to their age distributions, MFR components should be distinguishable by the elevation ranges at which they recharge, i.e., basin-floor elevations for surface MFR and higher elevations on the mountain block for diffuse MBR. To this end, noble gas thermometry, or the derivation of recharge temperature (T_r) based on the solubility behavior of noble gases, offers complementary information to age distributions. Provided a robust relationship between altitude and T_r is known or can be determined, noble gas concentrations dissolved in groundwater can be interpreted for the elevation at which recharge occurred, and are thus commonly employed in MFR studies (Althaus et al., 2009; Doyle et al., 2015; Gardner & Heilweil, 2014; Manning, 2011; Manning & Solomon, 2003). The relationship between air (T_a) and ground surface (T_s) temperature with elevation can be complicated in areas with seasonal snow cover (Bartlett et al., 2004). Determining the T_r lapse rate is yet more challenging due to a paucity of depth and temperature measurements of the regional water table (WT). Further, competing dynamics between the subsurface geothermal gradient and the amount and temperature of recharging water, such as that caused by snowmelt or focused recharge, could produce T_r lapse rates that deviate from T_s or T_a (Forster & Smith, 1989; Heilweil et al., 2012; Manning & Solomon, 2004). One promising avenue of addressing both issues is conducting numerical experiments of fluid and energy transport, which can be used to simulate plausible realizations of the system (Heilweil et al., 2012) and thus test the assumption of a constant T_r lapse rate under the influence of competing recharge dynamics.

This study combines multiple groundwater age tracers, including ^{85}Kr and ^{39}Ar , with noble gas thermometry and energy transport modeling to provide a rigorous, integrated approach for distinguishing and

quantifying MFR components. We use this approach to test the hypothesis that diffuse MBR is distinguishable and quantifiable from surface MFR and other recharge sources in basin-fill production wells by (a) age distributions substantially older than modern (e.g., post-1950s) water and (b) recharge elevation ranges higher than the basin floor. We use the Tucson Basin of southeastern, AZ, USA, a semiarid basin-fill aquifer system with a rich history of MFR investigations (Ajami et al., 2011; Cunningham et al., 1998; Eastoe et al., 2004; Kalin, 1994; Merz, 1985; Mohrbacher, 1984; Olson, 1982), to test this approach and hypothesis.

2. Site Description

The Tucson Basin, located in southeastern Arizona, is a semiarid extensional alluvial basin characteristic of the Basin and Range physiographic province. It is bounded by four mountain ranges: the Santa Catalinas to the North, the Rincon Mountains to the east, the Santa Rita Mountains to the south, and the Tucson Mountains to the west. Our study focuses on the northern Tucson Basin, encompassing the Santa Catalina mountains and a major portion of the Tucson basin-fill aquifer system (Figure 1a). Basin elevations range from ~800 m at the basin floor to ~2,900 m at the top of Mt. Lemmon. Mean annual precipitation varies strongly with elevation from 300 mm at the basin floor to >750 mm in the high mountains. High intensity convective summer monsoons occur July–September and lower intensity winter storms occur November–February, with total precipitation amounts roughly split between these periods (Ajami et al., 2011). Potential evapotranspiration greatly exceeds precipitation during summer months, leading to the majority of recharge occurring during winter when evapotranspiration demand is lower. Corroborating this, stable isotopes of groundwater consistently reflect winter precipitation in the Tucson basin-fill aquifer (Earman et al., 2006; Eastoe & Wright, 2019).

2.1. Hydrogeology

The Santa Catalina mountain block is comprised of igneous and metamorphic intrusive rocks. Importantly, the mountain front does not mark an immediate transition to a higher permeability basin-fill aquifer due to the presence of the consolidated gypsiferous Tertiary Pantano Formation (Figure 1). The major structural feature in this basin is the Catalina detachment fault, a low angle normal fault which formed during Neogene extensions, and is cut by high-angle normal faults (Davidson, 1973). These younger faults juxtapose the Pantano Formation against the Quaternary Fort Lowell and Tertiary Tinaja beds (i.e., the main basin-fill aquifer units). The Fort Lowell unit is the most productive in the basin-fill aquifer system. It grades from silty gravels near the unit margin to silty clays near the basin center and is ~100-m thick (Davidson, 1973). The Tertiary Tinaja Beds transition from silty gravels to silty mudstone at depth and range from 0 to 600 m in thickness from the margins toward the basin center (Davidson, 1973). Groundwater production wells are typically screened in the Upper Tinaja beds and Fort Lowell Formation. Four main ephemeral streams have eroded down through the Pantano Formation in the Santa Catalina piedmont, depositing permeable alluvium (“washes” in Figure 1a), which comprise “shoestring aquifers” connecting mountain streamflow to the basin fill (Belan, 1972).

3. Methods

3.1. Well Sampling and Analysis

Six wells were sampled in November 2018, four of which were production wells, one a shallow domestic well close to Sabino Creek, and one deep county well screened in the weathered bedrock (Figure 1b and Table 1). The four production wells and one bedrock well had been pumping for at least 12 h prior to sampling, and the domestic well was pumped for 1 h prior to sample collection. All samples were collected from a spigot prior to reaching the pressure tank and bottles were rinsed three times with the sample, filled with minimal headspace, wrapped with parafilm, and stored on ice, unless otherwise noted. Temperature, pH, electrical, and conductivity were measured and are reported alongside location, elevation, well depth, and screened interval in Table 1. Samples for alkalinity, anions, and cations were field-filtered using a 0.45- μ m nylon filter into HDPE bottles. Cation samples were field-acidified to a pH of 2. Unfiltered samples were collected for ^3H in 1 L HDPE bottles, and Carbon-13 ($\delta^{13}\text{C}$) of dissolved inorganic carbon (DIC) and ^{14}C in 1 L glass amber bottles sealed with electrical tape. Noble gases were collected using the copper tube method

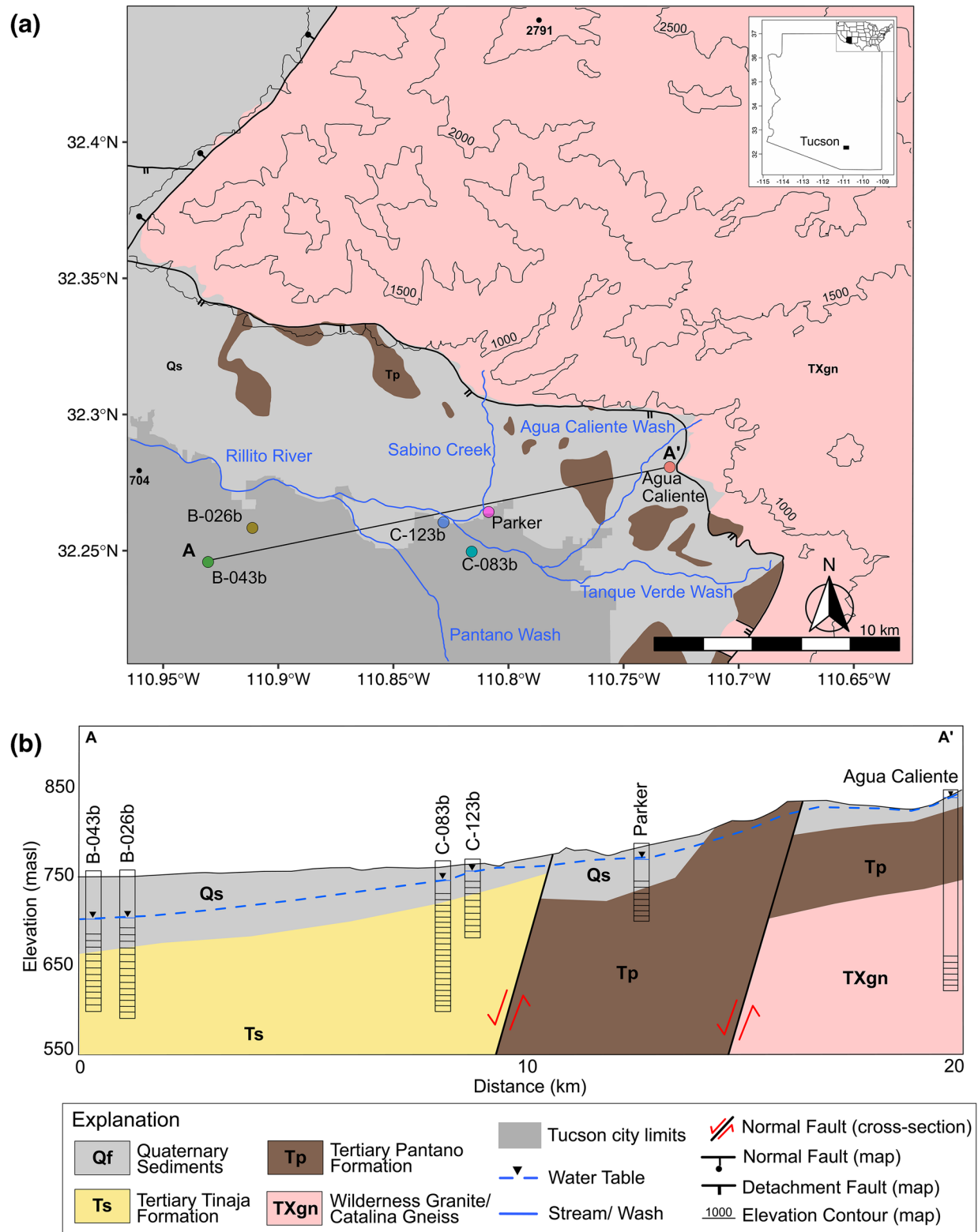


Figure 1. (a) Geologic map of the sample area including the general geologic units, major mapped faults, and six wells which roughly follow along a cross-section from A to A'. The same colors of the well symbols are used in subsequent plots and figures throughout the paper. Elevation contours (500 m) show the relief between the mountain block (max. 2,791 m) and the basin floor (min. 704 m). (b) Cross-section from A to A' showing the six wells sampled, including their screened intervals. The two normal faults are inferred from geologic mapping, and the subsurface contact between the igneous and metamorphic mountain block and the Pantano Formation is only known for the Agua Caliente well.

Table 1
Well Information, Including Depth to Water (DTW), and Field Parameters

Name	Date sampled	Longitude	Latitude	Elevation (masl)	Casing depth (m)	Screened interval (masl)	DTW (m)	pH	Temp. (C)	EC ($\mu\text{S}/\text{cm}$)	Pumping rate (gpm)
Agua Caliente	July 11, 2018	−110.73	32.28	833	244	632–589	10	8.13	34.0	266.3	7
Parker	May 11, 2018	−110.81	32.26	768	91	724–676	21	6.4	21.8	210.8	—
B-026b	May 11, 2018	−110.91	32.26	739	162	678–580	50	7.4	23.0	462	7
C-123b	June 11, 2018	−110.83	32.26	760	91	734–668	13	7.9	21.1	388	7
C-083b	June 11, 2018	−110.81	32.25	774	195	725–585	24	7.2	20.3	215.4	7
B-043b	September 11, 2018	−110.93	32.25	743	181	672–587	58	8.1	29.8	100.8	7

following the University of Utah Noble Gas Lab's protocol (https://noblegaslab.utah.edu/_documents/services-pricing/cu_tube_sampling.pdf) and analyzed at the University of Utah Noble Gas Lab. Samples for ^{85}Kr and ^{39}Ar required degassing roughly 1.5 m^3 of water in the field using a 3 M hydrophobic membrane. The extracted raw gas was collected into alloy cylinders and shipped to University of Bern. During sampling of the second to last well (Agua Caliente), a tear in the pump diaphragm was discovered and a repair was attempted in the field. The repair was only partially successful, as some atmospheric contamination is apparent in both Agua Caliente and B-043b, indicated by the abundance of ^{85}Kr and absence of ^3H . Hence, a correction was applied to the noble gas radioisotope data for these two wells.

Alkalinity was determined within 24 h of sampling using the Gran Alk titration method with a precision of $\pm 0.6\%$ (Gieskes & Rogers, 1973). Anions were measured using a Dionex Ion Chromatograph (IC) model ICS-3000 using an AS23 analytical column with an analytical precision of $\pm 2\%$. Cations were measured using inductively coupled plasma optical emission spectrometry (Perkins Elmer, Optima 5300DV, ICP-OES) with an analytical precision of $\pm 3\%$. ^3H was analyzed using liquid scintillation spectrometry on a Quantulus 1220 Spectrometer with a detection limit of 0.5 TU and analytical precision of $\pm 0.16\text{--}0.24\text{ TU}$. $\delta^{13}\text{C}$ of DIC was analyzed using a ThermoQuest Finnigan Delta Plus XL, coupled with a Gasbench automated sampler, and was standardized relative to NBS-22 with an analytical precision of $\pm 0.3\text{‰}$. ^{14}C was measured by Accelerator Mass Spectrometry, with a precision of $\pm 0.2\text{‰}$, in the NSF-Arizona Accelerator Facility. Ar and Kr were separated by large volume GC methods and ^{85}Kr and ^{39}Ar were measured using low level gas proportional counting in the Deep Laboratory of the Physics Institute, University of Bern, Switzerland (Loosli, 1983; Riedmann & Purtschert, 2016).

3.2. Tracer Interpretation

A measured tracer concentration, $C(t)$, can be interpreted for transit time, assuming steady-state groundwater flow, given the convolution integral (Maloszewski & Zuber, 1996)

$$C(t) = \int_0^\infty C_{in}(t-t')g(t')\exp(-\lambda t')dt' \quad (1)$$

where C_{in} is the tracer concentration at $t-t'$, the time of entry, t' is the transit time of the water parcel, $g(t')$ is a weighting function, and λ is the decay constant. The input function C_{in} varies between radioisotopes and geographic location as shown in Figure 2.

Measurements of amount-weighted ^3H in precipitation have been recorded in Tucson since the 1960s. While the bomb peak has largely decayed, measurement of ^3He (Schlosser et al., 1988), and interpretation of modern transit times (Morgenstern et al., 2010) from the modern background value of $5.3 \pm 0.3\text{ TU}$ (amount-weighted annual mean from 2001 to 2012 from Eastoe et al. (2012)) continues to make ^3H a viable tracer for modern

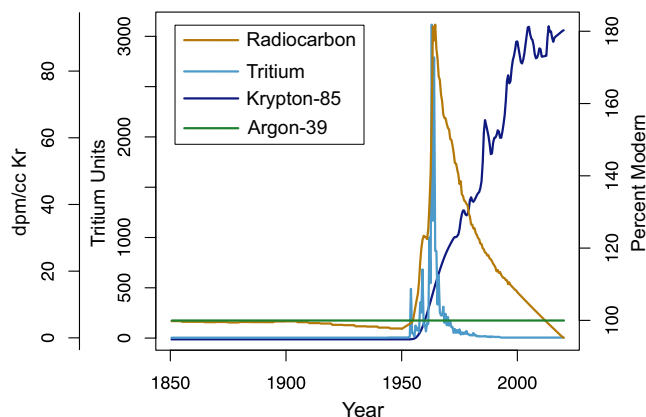


Figure 2. Input functions for radiocarbon, tritium, argon-39, and krypton-85 from 1850 to recent. Tritium is based on monthly weighted averages from Tucson, AZ (Eastoe & Dettman, 2016).

groundwater in Tucson. ^{39}Ar is produced in the atmosphere by cosmic rays and has remained somewhat constant with an activity of $1.67 \times 10^{-2} \text{ Bq/m}^3$ of air over time (Loosli, 1983; Loosli et al., 2000). This value translates to $1.78 \times 10^{-6} \text{ Bq/cm}^3$ STP of argon, which is expressed as 100% modern. Decreases from this value occur via radioactive decay with a half-life of 269 years, though this decrease can be suppressed by subsurface production of ^{39}Ar by the nuclear reaction $^{39}\text{K}(\text{n,p})^{39}\text{Ar}$ where the neutrons originate from U-Th decay (Corcho Alvarado et al., 2007; Loosli et al., 2000; Šrámek et al., 2017). The input function for ^{14}C was constructed from the international calibration curve, IntCal90 (Reimer et al., 2009), with ^{14}C concentrations from zone 2 of the northern hemisphere (Hua & Barbetti, 2004), and a modern ^{14}C concentration of 105 percent modern carbon (pMC) determined by several studies in the Tucson Basin (Eastoe et al., 2004; Hopkins et al., 2014). ^{85}Kr , expressed in this study as decays per minute (dpm) per cm^3 Kr, is also produced by cosmic rays in the atmosphere, however, a much larger anthropogenic source, specifically reprocessing of nuclear fuel rods, has led to the steady increase in ^{85}Kr in the atmosphere since the 1950s (Loosli et al., 1989). As the majority of this concentration is located in Central Europe, this study used a baseline input function for ^{85}Kr , developed by Bollhöfer et al. (2019) for distal geographical locations (Figure 2).

While $g(t')$ is typically not known a priori, numerous lumped parameter models (LPM) have been developed to represent physical processes of recharge and flow path capture by wells, and each can be solved analytically for the tracer-based age distribution (Jurgens et al., 2012; Maloszewski & Zuber, 1996). This study considers three LPMs. First, the piston flow model (PFM), which assumes no dispersion or mixing and a weighting function given by the Dirac delta (δ) function

$$g(t') = \delta(t' - \tau) \quad (2)$$

where τ is the piston flow age of the sample. Second, the exponential mixing model (EMM), which assumes no dispersion, a flow-weighted mixture of all flow paths, and a logarithmic age depth profile

$$g(t') = \frac{1}{\tau} e^{-\frac{t'}{\tau}} \quad (3)$$

where τ is the mean age of the sample. And third, a binary mixing model (PFM-EMM) combining a PFM and EMM model

$$C_{\text{out}} = f_1 C_1 + (1 - f_1) C_2 \quad (4)$$

where f_1 is the fraction of older water, C_1 is the tracer concentration for the older fraction, and C_2 is the tracer concentration for the modern PFM (Jurgens et al., 2012). For the binary models, three parameters must be either input or solved: the PFM age of the young component, the mean EMM age of the old component, and fraction of the old component. Diagnostic tracer-tracer plots and closed-form, analytical solutions for the probability density function and cumulative density function of groundwater age in the Tucson wells were performed using Tracer LPM (Jurgens et al., 2012). Best-fit parameters (mean age and modern fraction) were determined for the PFM and EMM by minimizing the χ^2 function

$$\chi^2 = \sum_i \frac{(C_i - C_i^{\text{mod}})^2}{\sigma_i^2} \quad (5)$$

where C_i is the measured concentration for each tracer i , C_i^{mod} is the modeled concentration, and σ^2 is the squared laboratory analytical and sampling error.

Prior to interpreting ^{14}C for groundwater age using LPMs, a correction was applied using the geochemical flow path modeling and radiocarbon correction code, NETPATH (Plummer et al., 1994). This is necessitated by the complex geochemical processes occurring along a flow path that can alter the final ^{14}C activity, in most cases resulting in an erroneously lower activity and older age. The assumptions, phases, and constraints used in the NETPATH modeling are discussed in detail in the supporting information. Importantly, error associated with geochemical correction has been shown to be 100 times greater than analytical error for ^{14}C ($\sim 0.1 \text{ pmc}$) (McCallum et al., 2018). As a full Monte Carlo error analysis with NETPATH modeling

is beyond the scope of this study, we assign an error of 10 pmc to all ^{14}C activities in order to mitigate undue weight given to the tracer during optimization.

Finally, quantitative estimates for MFR components are calculated using the following equations:

$$v = \frac{q}{n_e} \quad (6)$$

$$Q = q * A \quad (7)$$

where v is water velocity (L/T), q is the specific discharge (L/T), n_e is the effective porosity, Q is the volumetric flux (L^3/T), and A is the cross-sectional area (L^2). The distance is assumed to be the shortest distance to the median noble gas-derived recharge elevation (discussed below) from the well, and the effective porosity and cross-sectional area vary based on each individual well.

3.3. Noble Gas Interpretation

Noble gases have long been recognized as useful tracers in meteoric waters, because they are ubiquitous and inert, and for all except helium, have no appreciable sources besides the atmosphere (Kipfer et al., 2008). This study accounted for nonatmospheric sources helium based on the equations in the Appendix of Schlosser et al. (1989), described in further detail in the supporting information. In groundwater, noble gases are almost always dissolved in excess of equilibrium and various empirical models have been developed to account for this excess air component (Aeschbach-Hertig et al., 1999). This study considers the Closed system Equilibration (CE) model (Aeschbach-Hertig et al., 2000; Jung et al., 2013)

$$C_i(S, T, P, A_e, F) = C_i^{eq}(S, T, P) + \frac{(1 - F) \cdot A_e z_i}{1 + \frac{F A_e z_i}{C_i^{eq}}} \quad (8)$$

where S is salinity, T is temperature of the water table, P is pressure, A_e is the initial volume of gas per unit volume of porous media in $\text{cm}^3 \text{ STP/g}$, z_i is the volume fraction of individual gases in dry air, and F is a dimensionless parameter describing the reduction in the trapped gas volume during reequilibration. The CE model is often the preferred excess air model for noble gas interpretation, because the parameters represent physical conditions during gas exchange and because noble gases appear to most often exhibit CE-type fractionation (Kipfer et al., 2008).

Given the measured concentrations of Ne, Ar, Kr, and Xe, a system of equations can be solved simultaneously for unknown parameters T , A_e , and F by minimizing the χ^2 function (Equation 5). If recharge elevation is also unknown, then the inverse solution is ill-posed; however, several studies have pointed out that this method could be used to solve for the sample lapse rate, or the decrease in recharge temperature with decreasing pressure (increasing elevation), by assuming a minimum and maximum pressure and solving for temperature (Aeschbach-Hertig et al., 1999; Ballentine & Hall, 1999; Manning & Solomon, 2003). These serve as the upper and lower limits for all potential combinations of temperature with pressure for each sample. Where this sample line crosses the recharge temperature (T_r) lapse rate can be interpreted as the median recharge elevation (Doyle et al., 2015; Heilweil et al., 2012; Manning & Solomon, 2003; Peters et al., 2018). One approach in determining the T_r lapse rate is to assume that it is approximately equal to the atmospheric temperature (T_a) lapse rate, however as Manning and Solomon (2003) thoroughly discuss, this assumption is often violated for two reasons: (1) mountain water tables are often recharged by snowmelt, which results in $T_r < T_a$ and (2) deeper water tables may not receive high enough recharge rates to suppress the geothermal gradients within mountain blocks, which would result in $T_r > T_a$.

This study considers both the T_a and ground surface temperature (T_s) lapse rate for recharge elevation estimation. The T_s lapse rate was established by measuring temperatures in eight springs in May 2019 ranging from 1,634 to 2,724 masl in the Santa Catalina mountains, as well as one shallow well at the basin floor (768 masl). A χ^2 minimization was performed to solve for T , A_e , and F for the two fixed pressure models with 10,000 Monte Carlo (MC) realizations each using the Panga software tool (Jung & Aeschbach, 2018).

Table 2
Flow and Heat Transport Parameters for the Base Case

Unit	K (m/s)	Porosity (%)	S_s (1/m)	RMC (%)	$K_{t,r}$ (W/m °C)	$K_{t,s}$ (W/m °C)
Unweathered bedrock	5×10^{-9}	6	1×10^{-6}	0.02	2.8	3.0
Weathered bedrock	8×10^{-7}	10	1×10^{-5}	0.02	1.8	2.2
Pantano Formation	5×10^{-6}	12	5×10^{-5}	0.03	1.8	2.2
Basin fill	5×10^{-5}	20	1×10^{-4}	0.03	1.8	2.2

Note. K = hydraulic conductivity, S_s = specific storage, RMC = residual moisture content, $K_{t,r}$ = thermal conductivity at residual moisture content, and $K_{t,s}$ = thermal conductivity at saturation.

Since the results from these two CE-models bound the range of recharge temperatures and consequently the range of recharge elevations for each sample, a straight line connecting the minimum and maximum pressure T_r represents all possible T_r -elevation pairs. Where this sample line intersects the true T_r lapse rate, which can be assumed to be constant or allowed to vary, provides the likely median recharge elevation.

3.4. Energy Transport Modeling

The variation of T_r with elevation is key for interpreting NGTs for recharge elevation, but in the case of the Santa Catalina mountains, T_r is not well constrained. This is due to a lack of deep boreholes or tunnels in the mountain block from which to measure the temperature at the water table. T_s determined from springs is likely cooler than the deeper water table, since recharge rates in this semiarid system are not high enough to suppress the geothermal gradient at depth. This study hypothesizes that high surface MFR rates may suppress water table temperatures substantially in the basin-fill aquifer. To test this, we ran numerical experiments using VS2DH, a variably saturated, two-dimensional groundwater flow, and heat transport model (Healy, 1990; Healy & Ronan, 1996; Lappala et al., 1987). VS2DH solves 2D groundwater flow using the Richards' equation and energy transport using an analog to the advection-dispersion equation of solute transport (Healy & Ronan, 1996)

$$\nabla S = \nabla \cdot K_T (\theta) \nabla T + \nabla \cdot C_w D_H \nabla T - \nabla \theta C_w v T + q_f C_w T^* \quad (9)$$

where ∇S is the change in heat storage, K_t is the thermal conductivity of the water and solid matrix in W/m °C, θ is the volumetric moisture content, T is the temperature in °C of the porous media volume, C_w is the heat capacity of water in J m⁻³ °C⁻¹, D_h is the hydrodynamic dispersion tensor in m²/s, v is water velocity in m/s, q_f is the rate of fluid source in 1/s, and T^* is the temperature of fluid source in °C. The right-hand side of Equation 9 can be interpreted as follows: the first term represents thermal conduction, the second term represents energy transport due to thermomechanical dispersion, the third term represents heat advection, and the fourth term accounts for sources and sinks (Healy & Ronan, 1996). Importantly, VS2DH assumes isotropic thermal conductivity and does not include temperature effects on density; however, it does allow hydraulic conductivity to vary as a function of temperature by way of the dependence of viscosity on temperature (Kipp, 1987).

The 2D model represents a transect from the highest point in the Santa Catalina mountains (Mt. Lemmon) to the basin floor. Figure 3 shows the base model, geologic units, and boundary conditions, and Table 2 provides the parameter values that were varied between the units. The domain is discretized with $dx = 250$ m, $dz = 100$ m, resulting in 100 columns and 30 rows with a maximum thickness of 3,000 m at the top of Mt. Lemmon and a minimum thickness of 700 m at the basin floor. The K values and ranges for mountain units were obtained from Welch and Allen (2014), and K values and ranges for the Pantano Formation and basin-fill units were taken from the existing Tucson active management area MODFLOW model (Mason & Hipke, 2013). The K value for the unweathered bedrock was assumed to be isotropic, whereas the K_x/K_z values for the other units was set to 10. Mountain aquifer recharge was taken to be 2% of annual precipitation, varying from 5×10^{-10} m/s at high elevations to 2×10^{-10} m/s at the basin floor (Figure 3). This value

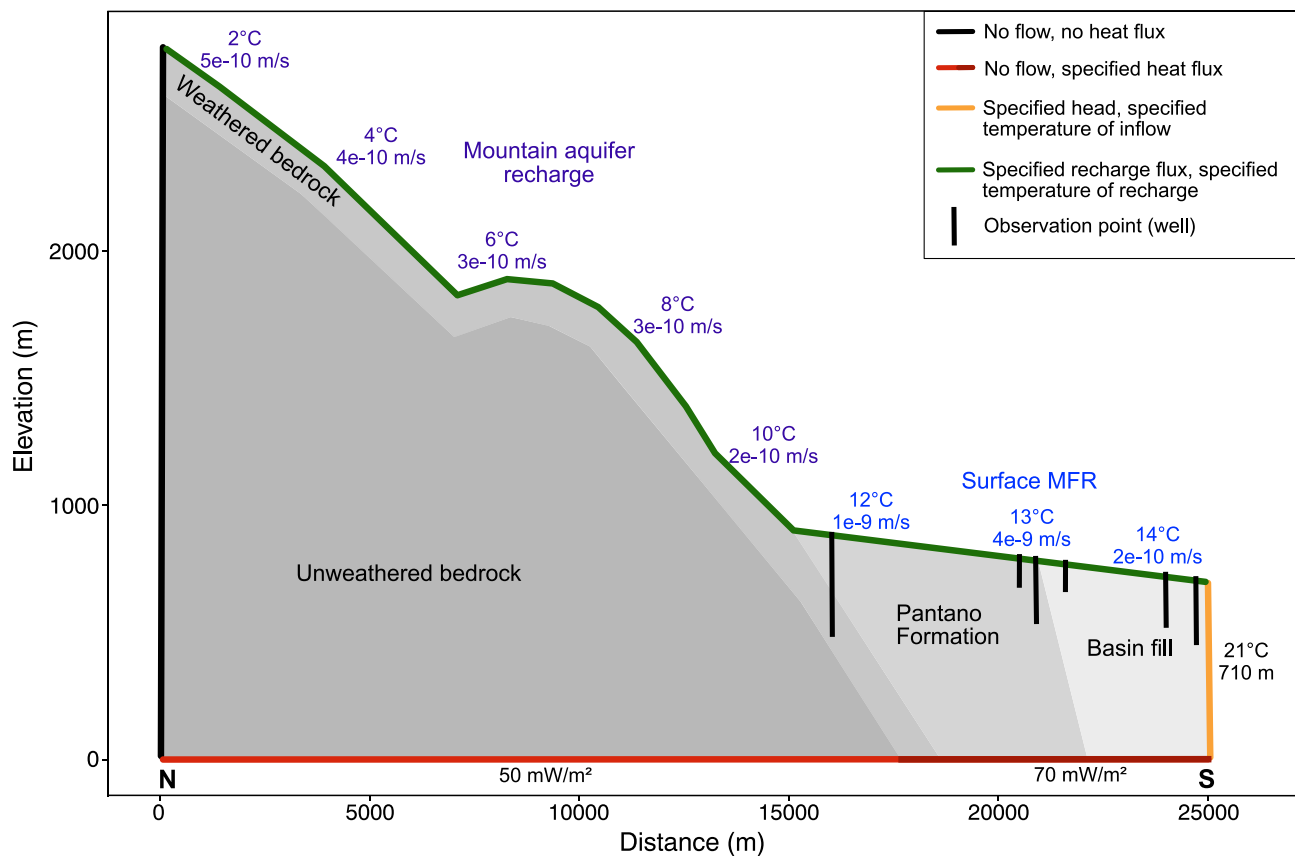


Figure 3. Schematic diagram of the VS2DH transect model, showing the different geologic units (grayscale), and the hydraulic and thermal boundary conditions. The vertical black lines show the approximate location and depth of observation points used to compare to measured temperatures in the wells. Note that the modeled cross-section is oriented N-S along the dominant direction of groundwater flow, and so well locations were determined along that 2D transect as opposed to the cross-section in Figure 1.

of 2% is slightly higher than the values estimated from Ajami et al. (2011) and Dwivedi et al. (2019), which estimated around 1% of precipitation becomes mountain aquifer recharge, however both studies occurred across limited modern time spans and likely reflect a dry tendency in the recent (<10 years) precipitation record for southern Arizona. The surface MFR rates were taken from the estimates reviewed in Carlson et al. (2011), which range from 0.15 to 6.0×10^6 m³/km/year for the Rillito River. The basal heat flux of the mountain block was set to 50 mW/m², reflecting the lower heat fluxes associated with metamorphic core complexes in Arizona (Lachenbruch et al., 1994). A basal heat flux of 70 mW/m² was assigned beneath the Pantano and basin-fill aquifer units based on heat flow maps produced by Sass et al. (1994).

Nine scenarios were simulated to test a range of conceptualizations of groundwater flow and heat transport: (1) a base case with the parameters described above and in Table 2; (2) more recharge, where all recharge fluxes were increased by 50%; (3) less recharge, where all recharge fluxes were decreased by 50%; (4) colder recharge, where the temperature of recharge was decreased by 2 °C; (5) warmer recharge, where the temperature of recharge was increased by 7 °C, roughly equaling the average annual air temperatures in the Tucson Basin; (6) higher K , where all K values are increased by a factor of 10; (7) lower K , where all K values are decreased by a factor of 10; (8) more river recharge, where only the surface MFR fluxes are increased by 50%; and (9) more mountain aquifer recharge, where recharge fluxes to the mountain block are increased by 50%. Scenario plausibility was assessed by comparing modeled temperatures to measured spring and production well temperatures. The spring temperatures were taken to be the temperature at the land surface in the model, and the temperatures measured during well sampling were taken to be the screen midpoint depth. The modeled T_r was taken to be the temperature of the water table at each land surface grid cell elevation in the model.

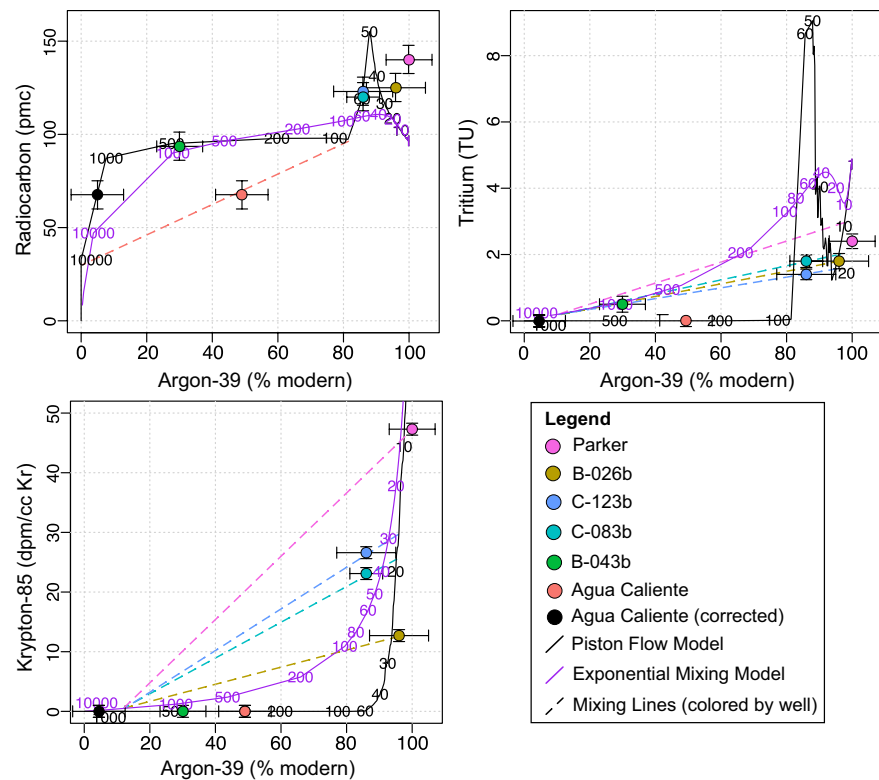


Figure 4. Tracer-tracer plots showing the expected concentrations for the piston flow and exponential mixing models in black and purple, respectively, as well as the PFM-PFM and PFM-EMM dashed mixing lines colored by well (corresponding to Table 3). PFM, piston flow model; EMM, exponential mixing model.

4. Results

4.1. Age Modeling

All wells except for Agua Caliente contained measurable ^3H and ^{85}Kr , indicating that they are receiving some modern recharge (Table 3). In general, the piston flow ages estimated from ^3H , ^{85}Kr , and, when present, ^3He agreed within a few years (Table 3). Mean piston flow ages increased with increasing depth of groundwater production (Table 1), indicating a general age stratification with depth commonly found in unconsolidated aquifers (Schlosser et al., 1989; Visser et al., 2013; Vogel, 1967). Of the six, only two wells showed premodern ^{14}C concentrations, while the other four wells showed evidence of bomb-derived radiocarbon (Table 3), indicating that produced groundwater in the study area is predominantly modern. While nonatmospheric ^4He was detected in four of the samples (Table 3), parsing the crustal, mantle, and external sources required for an age interpretation (Castro et al., 2000) was beyond the scope of this study and thus $^4\text{He}_{\text{terr}}$ was not used in the lumped parameter modeling. Further details on the calculation of helium components can be found in the supporting information.

Two lines of evidence support the wells capturing a mixture of flow paths. First, several wells containing detectable ^3H also contain terrigenic helium, which is a product of U/Th decay and generally indicates the presence of older water (Solomon, 2000). And second, the piston flow ages determined from ^{39}Ar indicate the presence of water that is older than predicted from the modern tracer data in several wells. We present the tracer and LPM results organized by each individual well.

Agua Caliente—The groundwater at this well possessed the lowest concentration of corrected ^{14}C and had no detectable tritium (Figure 4), indicating that it is capturing entirely premodern water. However, the relatively high presence of ^{85}Kr (16.6 dpm/cm³ Kr), which has a half-life of 10.74 years (Sing & Chen, 2014), suggests that there was contamination during sampling for the two dissolved noble gas radioisotopes. If the ^{85}Kr concentration is used as a correction indicator and a modern air concentration of 78 dpm/cm³ Kr

Table 3
Tracer Concentrations and PFM Ages Estimated From TracerLPM

Well	^3H		$^3\text{He}_{\text{trit}}$	$^4\text{He}_{\text{terr}}$	$^3\text{H}/^3\text{He}_{\text{trit}}$		^{85}Kr		^{39}Ar		^{14}C (raw)	^{14}C (corrected)	
	TU	years	TU	$\times 10^{-7} \text{ cm}^3$ STP/g	years		dpm/cm ³ Kr	years	% modern	years	pmc	pmc	years
Agua Caliente	BDL	—	—	49.0	—		0.0 ^a	— ^a	49 ± 8 ^a	270 ± 60	41 ± 10	67 ± 10	3,400 ± 1,600
B-026b	1.8 ± 0.23	16 ± 1	—	1.0	—		12.7 ± 1.0	22 ± 1	96 ± 9	16 ± 30	85 ± 10	115 ± 10 ^b	36 ± 8
B-043b	0.5 ± 0.24	55 ± 1	—	3.9	—		0.0 ^a	— ^a	30 ± 7 ^a	290 ± 50	48 ± 10	93 ± 10	600 ± 800
C-083b	1.8 ± 0.19	16 ± 1	3.7 ± 0.19	—	20 ± 1		22.7 ± 1.0 ^c	16 ± 1 ^c	84 ± 7 ^c	60 ± 20 ^c	88 ± 10	120 ± 10 ^b	33 ± 6
C-123b	1.4 ± 0.16	16 ± 1	1.7 ± 0.16	—	14 ± 1		26.6 ± 1.0	14 ± 1	86 ± 9	60 ± 40	88 ± 10	123 ± 10 ^b	36 ± 8
Parker	2.4 ± 0.22	13 ± 1	—	0.9	—		47.3 ± 1.0	8 ± 1	100 ± 7	Modern	103 ± 10	140 ± 10 ^b	45 ± 8

^aFollowing correction for the 16.6 dpm/cm³ Kr determined to be from contamination of modern atmospheric air (78 dpm/cm³ Kr). ^bThe presence of bomb-derived ¹⁴C. ^cMean of duplicate value.

is assumed, the corrected ³⁹Ar concentration is still 49% ± 9 modern, which results in a piston flow age of 270 ± 60 years. With the correction applied, the best-fit LPM for Agua Caliente is a binary piston flow mixing model (Figure 4, dashed line). The piston flow age of the “old” component was estimated from a previous study which determined a radiocarbon age for a nearby well of 12,000 years (Kalin, 1994). The “young” component was estimated by the model, with the constraint that it be premodern due to the absence of tritium. The resulting mixing fractions of the two components are 42% old and 58% modern (Table 4).

Even with the correction applied, the ³⁹Ar concentration is higher than would be expected given the ¹⁴C age and abundance of terrigenous helium (Table 3). One possible explanation for the elevated concentration found in this well is nucleogenic subsurface production of ³⁹Ar related to neutrons originating from U/Th decay (Šrámek et al., 2017). Subsurface production is especially common in granitic systems and hydrothermal systems (Yokochi et al., 2012); e.g., Loosli et al. (1989) documented ³⁹Ar activities in excess of atmospheric (>100% modern) in the Stripa granite of Sweden. Following the approach described in Lehmann and Loosli (1991), we estimated a range of nucleogenic activities of ³⁹Ar based on measurements of U, Th, and K concentrations, porosity, and escape rates from the rock to groundwater. These data and calculations are described in detail in the Supporting Information. Resulting estimated activities of nucleogenic ³⁹Ar range from 15% to 350% modern using an escape rate of 0.6% and 3.8% and porosities of 2% and 0.5%, respectively. Thus, it is plausible that the majority of ³⁹Ar present in the Agua Caliente sample is from in situ production. For this reason, we tested a second age modeling scenario for Agua Caliente (Table 4) where the activity of atmospheric ³⁹Ar is equal to the detection limit (5 ± 8% modern). The best-fit LPM for this scenario is an EMM, with mean age of 4,300 years (Table 4). This age distribution implies a large upgradient area receiving uniform recharge producing an infinite number of flow paths, commonly found in flow path convergence in a watershed to a spring (Cook & Böhlke, 2000). Given that the Agua Caliente well is located at the mountain front and meters from Agua Caliente spring, there is better conceptual support for this model result and thus an EMM with mean age of 4,300 was used to represent the old groundwater component for binary mixing in the downgradient wells.

Parker—The groundwater at this well had the highest concentrations of all tracers (Figure 4), indicating it is capturing predominantly modern water. This is not surprising as it is the shallowest well with a short screen predominantly occurring in the permeable fluvial unit (Figure 1b) and is located close to Sabino Creek (Figure 1a). That being said, roughly 40% of the helium concentration in the groundwater at this well is terrigenous (Table 3). This presence of terrigenous helium could arise from mixing between modern and old waters. Ignoring the terrigenous helium results in a best-fit PFM age distribution with an age of 10 years. Accounting for the terrigenous helium, a binary mixing model of a modern PFM component and the old component represented by the Agua Caliente EMM results in a 1% fraction of old water (Table 4).

Wells C-123b and C-083b—Tracer concentrations and LPM results show potential mixing behavior between modern surface MFR and older diffuse MBR for these two wells (Figure 4). Piston flow ages for ³H, ³H/³He, and ⁸⁵Kr agreed well, and were roughly 16 years, while the ³⁹Ar concentrations gave a slightly different

Table 4
Best-Fit Age Model, Mean and PFM Ages, and for the Binary Mixing Models Fraction “Old” Water (f_1 From Equation 4)

Well	Age model	Tracers	Mean EMM or PFM age (years)	Modern component age (years)	Old component age (years)	f_1 (%)
Agua Caliente	PFM-PFM	^{39}Ar , ^{14}C , ^3H , ^{85}Kr	—	76 ± 83	12,000 ^a	$42 \pm 12\%$
	EMM	^{39}Ar , ^{14}C , ^3H , ^{85}Kr	$4,300 \pm 2,000$	—	—	—
B-026b	PFM	^{39}Ar , ^{14}C , ^3H , ^{85}Kr	25 ± 1	—	—	—
	PFM-EMM	^{39}Ar , ^{14}C , ^3H , ^{85}Kr	—	25 ± 1	4,300 ^a	$1 \pm 6\%$
B-043b	EMM	^{39}Ar , ^{14}C , ^3H , ^{85}Kr	$1,000 \pm 260$	—	—	—
C-083b	PFM-EMM	^{39}Ar , ^{14}C , ^3H , ^{85}Kr	—	18 ± 1	4,300 ^a	$7 \pm 8\%$
C-123b	PFM-EMM	^{39}Ar , ^{14}C , ^3H , ^{85}Kr	—	16 ± 1	4,300 ^a	$6 \pm 10\%$
Parker	PFM	^{39}Ar , ^{14}C , ^3H , ^{85}Kr	9 ± 1	—	—	—
	PFM-EMM	^{39}Ar , ^{14}C , ^3H , ^{85}Kr	—	10 ± 1	4,300 ^a	$1 \pm 8\%$

The modern component is a PFM age whereas the old component can be a PFM age or an EMM mean age, depending on the age model of the well.

^aAn initial value, which was not estimated as a parameter by the LPM.

result of 85% modern, indicating a piston flow age of 60 years (Table 3). For this reason, the most suitable LPMs were both binary mixtures of mostly modern and some premodern water. For this mixing problem, the EMM mean age from Agua Caliente (4,300 years) was used as an initial value in TracerLPM optimization. The best-fit LPM for groundwater at C-083b was a binary mixing model (PFM-EMM), with a modern (18 years) component, an old component, and a fraction of 7% old (Table 4). Groundwater located at C-123b showed a slightly younger modern piston flow age (16 years) and a slightly smaller fraction (6%) of old water.

Well B-026b—Groundwater at this well showed good agreement between all tracers for uniform, modern-aged water (Table 3); however, the presence of terrigenous helium suggests mixing with a small amount of old water is occurring. Similar to the Parker well, there are two potential explanations for the observed tracer concentrations. Ignoring terrigenous helium, the best-fit LPM for B-026b is a piston flow model with a uniform age of 25 ± 1 year (Table 4). Accounting for helium via mixing with an old component of water taken from the Agua Caliente exponential distribution results in a negligible fraction (1%) of old water. This result is somewhat surprising given the long-screen and deep completion, and we offer our hypothesis in the discussion.

Well B-043b—This well has similar completion characteristics as well B-026b (Figure 1b) but is located furthest from the mountain front of all wells, toward the center of the basin-fill aquifer. As such, well groundwater at B-043b showed the strongest mixing of tracer concentrations (Figure 4), with premodern ^{14}C and ^{39}Ar concentrations and a ^3H concentration equal to the detection limit (Table 3). Similar to the Agua Caliente well, this well had a ^3H concentration that was almost nondetectable (0.05 TU), but a ^{85}Kr concentration (16 dpm/cm³ Kr) indicating modern groundwater. We conclude that this is indicative of contamination during sampling, and the correction results in a ^{39}Ar activity of $30 \pm 8\%$ modern. The best-fit LPM for B-043b is an exponential mixing model with a mean age of $1,000 \pm 260$ years (Table 4).

4.2. Noble Gas Thermometry

The measured concentrations of noble gases and CE-model results are presented in Table 5. Positive ΔNe values indicate that groundwater located at all the wells contained excess air, and very high ΔNe such as in Parker and B-026b is often accompanied by degassing. The χ^2 values and associated probabilities indicate that the CE-model fit the data reasonably well. In some cases, however, the MC analysis resulted in two local minima in the χ^2 surface for the parameters A_e and T , resulting in large parameter uncertainty for each. In these cases, we restricted the MC analyses to the range of realistic values for A_e (e.g., <0.1 cm³/g STP) and T following recommendations by Jung et al. (2013). The resulting T_r when assuming maximum

Table 5
Noble Gas Data and CE-Model Results

Well	Ar 10^{-4}	Kr 10^{-8}	Ne 10^{-7}	Xe 10^{-8}	^3He 10^{-13}	^4He 10^{-7}	ΔNe (%)	R/Ra	χ^2	Pr (χ^2) %	F	A_e	$T_{r,max}$ (°C)	$T_{r,min}$ (°C)
Agua Caliente	2.98	6.33	1.87	0.855	3.80	49.5	16	0.055	0.221	63.82	0.836	0.047	21.39	15.41
B-026b	5.75	10.6	4.19	1.28	1.22	2.22	154	0.403	0.817	36.58	0.338	0.102	20.03	12.81
B-043b	3.58	7.37	2.34	0.989	8.11	4.54	40	0.128	0.304	58.14	0.644	0.038	18.60	12.45
C-083b	5.11	9.10	3.93	1.18	1.03	0.687	137	1.087	3.162	7.53	0.326	0.055	18.50	12.18
C-123b	4.09	8.07	2.64	1.05	0.700	0.482	61	1.048	1.282	25.74	0.583	0.095	20.34	13.98
Parker	5.65	9.84	5.21	1.23	1.51	2.30	209	0.475	1.521	21.75	0.176	0.042	16.97	10.81

^3Ar , Kr, Ne, Xe, ^3He , ^4He , and A_e concentrations are reported in cm^3 STP/g. Analytical errors are 2%, 4%, 2%, 4%, 1%, and 1% for the six noble gases, respectively.

pressure (corresponding to minimum elevation) were all cooler than the measured sampling temperatures, particularly for groundwater at the Agua Caliente well (Table 1). The resulting T_r when assuming minimum pressure (corresponding to maximum elevation) were cooler than $T_{r,max}$ predictably, however, they were several degrees warmer than those predicted by the T_s and T_a lapse rates (Figure 5).

4.3. Recharge Elevations

4.3.1. Recharge Elevations Assuming a Constant Lapse Rate

The MC model results include a distribution of T_r 's estimated with the CE model (Jung & Aeschbach, 2018), which translates to a range of recharge elevations via intersection with the T_r lapse rate. For simplicity's sake, we present the median of these distributions as the “most likely” recharge elevation, but each of the recharge temperatures have an uncertainty of roughly 2 °C and corresponding elevation uncertainty of several hundreds of meters (Figure 5). Assuming a constant T_r lapse rate equal to either the ground surface or air temperature lapse rate (T_s and T_a , respectively) resulted in similar median recharge elevations for wells B-026b, C-083b, C-123b, and B-043b of around 1,250 masl (Figure 5). The Parker well median recharge elevation was 1,700 and 2,000 m assuming T_r equal to T_s and T_a , respectively (Figure 5, pink). The Agua Caliente well, on the other hand, fell right on the lapse rate line for T_a , meaning the median recharge elevation is equal to the wellhead elevation, and its intersection with the T_s lapse rate resulted in a median recharge elevation of 1,000 m (i.e., the lowest recharge elevation of all groundwater sampled in the study).

4.3.2. Recharge Elevations Using the VS2DH Modeled Variable Lapse Rate

The VS2DH transect models are employed in this study to test the hypothesis that snowmelt-derived surface MFR could suppress NGTs in the basin-fill aquifer system. We present the results as modeled vs. observed temperatures in order to demonstrate the sensitivity and uncertainty in the main model parameters; however, these numerical experiments were not calibrated. Also worth noting is that the regional water table in the mountain block is likely deeper than the soil and shallow groundwater flow paths feeding the ephemeral springs measured for this study (Dwivedi et al., 2019); however, the model can estimate temperatures for these springs owing to its ability to solve for flow and energy transport in variably saturated conditions. Model plots of the steady-state water table configuration, temperature distribution, and head contours can be found in the supporting information.

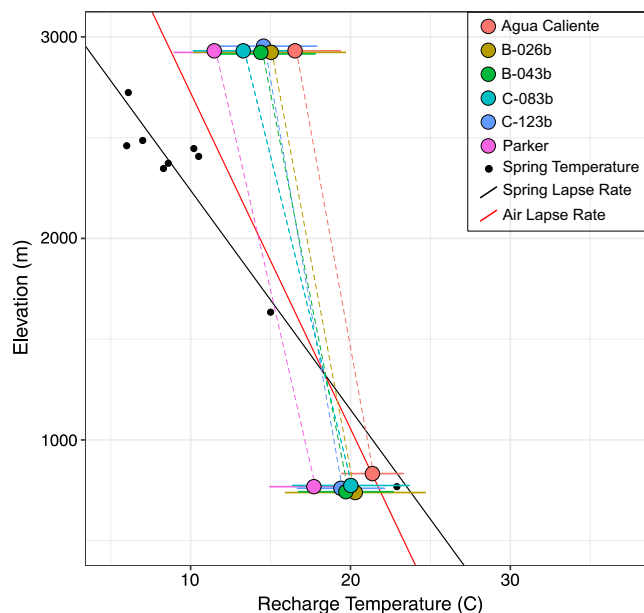


Figure 5. Noble gas recharge temperatures from the closed equilibrium model assuming minimum pressure (top of Mt. Lemmon) and maximum pressure (well head elevation) are given by the colored circles. Note the upper points are adjusted slightly to ensure that the points and error bars are visible. The filled circles and horizontal error bars signify the median and 95% confidence intervals of the 10,000 Monte Carlo simulations for the two fixed pressure models. The measured spring temperatures are plotted in black along with the lapse rate determined from the spring data (solid black line, -8.5 °C per 1,000 m) and the Tucson air temperature lapse rate (-6 °C per 1,000 m) determined by Harlow et al. (2004) is shown by the red line. For clarity, we only show the median sample line connecting the T_r pairs (dashed lines); however, in reality there are ~ 2 °C of uncertainty with corresponding to several hundreds of meters uncertainty in recharge elevation.

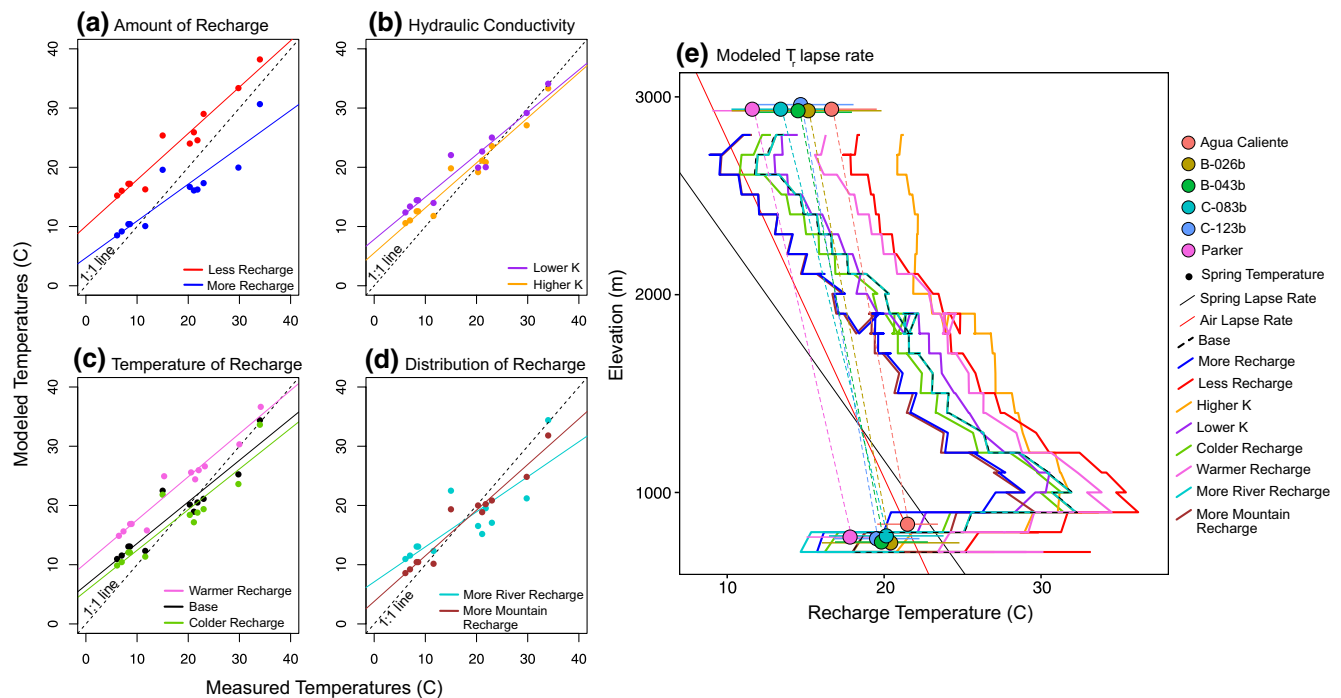


Figure 6. Sensitivity plots of modeled vs. measured temperatures for (a) specified recharge was increased (blue) and decreased (red) by 50%, (b) K was increased (orange) and decreased (purple) by an order of magnitude, (c) recharge was decreased by 2 °C (green) and increased by 7 °C (pink) relative to the base scenario (black), (d) recharge to the mountain block (brown) and to the basin floor (cyan) were increased by 50% and (e) modeled T_r lapse rates from all nine scenarios plotted along with CE-model results for noble gas T_r 's for the minimum and maximum pressure. The solid black line is the local ground surface temperature lapse rate (T_s) and the solid red line is the local air temperature lapse rate (T_a). A figure with all individual modeled T_r lapse rates plotted along with the CE-model results can be found in the Supporting Information.

In general, the models overestimated spring temperatures in the upper mountain block and underestimated production well temperatures in the basin-fill aquifer (Figure 6). Increasing or decreasing the recharge rate by 50%, well within uncertainty bounds of recharge for this transect, resulted in the largest differences in WT temperatures (Figure 6a). The more river recharge scenario predictably resulted in a decrease in basin-fill aquifer WT temperatures and conversely, the more mountain recharge scenario resulted in decreased WT temperatures in the mountain block (Figure 6d). Increasing the K of all geologic units by one order of magnitude produced a modest decrease in mountain WT temperatures and a modest increase in basin-fill aquifer temperatures relative to the base scenario (Figure 6b). The colder recharge scenario, in which the temperature of specified recharge was decreased by 2°C from the base scenario, resulted in a 1–2°C decrease of WT temperature for the observation points (Figure 6c). Conversely, increasing the temperature of recharge by 7°C resulted in a ~5°C increase in WT temperatures. These simulations demonstrate a dominant model sensitivity to recharge amount.

Taken together, the results from all nine modeled scenarios provide a reasonable approximation of the uncertainty and possible value of recharge temperatures for the transect (Figure 6e). Importantly, all modeled scenarios show a substantial decrease in WT temperatures in the basin-fill aquifer as a result of surface MFR, regardless of the temperature, K , or recharge amount. The modeled recharge temperatures across all scenarios show an average decrease of 10°C at the basin-floor elevation, and all but two intersect the CE-model results for the high pressure (low elevation) NGTs (Figure 6e). Although this model is highly simplified, the results suggest that the ranges of surface MFR fluxes in the Tucson basin-fill aquifer system might be the cause for the low NGTs in the sampled wells capturing modern groundwater.

Using the mean VS2DH T_r lapse rate, all sample T_r lapse rates except for Agua Caliente now cross the modeled T_r lapse rate twice, suggesting a nonunique median recharge elevation (Figure 6e). However, previous modeling work has shown that MBR in low permeability fractured crystalline systems is largely limited to near the mountain front, as front-slope flow (Manning & Solomon, 2005; Markovich et al., 2019; Welch &

Allen, 2014). This conceptual understanding allows for the elimination of the upper median recharge elevations, as they would require MBR to originate too far back in the mountain block. Thus, the model results suggest that the majority of recharge occurs at roughly the same elevation as the wells, which reduces the previous estimate of recharge elevations (Figure 5) by up to 1,000 m in the case of groundwater at the Parker Well and around 500 m for groundwater located at B-026b, B-043b, C-123b, and C-083b (Figure 6e). The only well that does not fall within the range of basin-floor elevation recharge is Agua Caliente. This is not surprising since this well is the most proximal to the mountain front, is entirely completed in weathered crystalline bedrock (Figure 1) and exhibited the oldest age distribution of all six wells (Table 4).

5. Discussion

5.1. Age Modeling

The first hypothesis we posed was that diffuse MBR should be distinctly older than surface MFR and thus detectable in an age distribution. Agua Caliente was the only well completed in the weathered bedrock, and groundwater sampled from it contained no measurable ^3H and exhibited a radiocarbon age that was distinctly older than the remaining five wells (Table 3), supporting the hypothesis that diffuse MBR will be substantially older than surface MFR. Groundwater collected from two of the four production wells exhibited binary age distributions of mostly modern and a small fraction of very old water, adding weight to the hypothesis that diffuse MBR can be detected and quantified in an age distribution (Table 4). However, even with a fairly continuous spread of age tracers, interpretation of age distributions from tracer concentrations remains uncertain and/or nonunique due to simplifying assumptions, sampling error, and analytical uncertainty (Figure 4).

For example, the true age distribution of the groundwater captured by the Agua Caliente well remains uncertain due to the relatively high ^{39}Ar activity. We posit that this could be entirely from subsurface production in the granitic bedrock (Lehmann & Loosli, 1991; Šrámek et al., 2017); however, the concentration of ^{39}Ar and porosity of the rock as well as escape rate to water are not well constrained. The absence of ^3H in Agua Caliente groundwater precludes modern recharge; however, mixing processes with intermediate-aged (~ 100 years) water containing atmospheric ^{39}Ar cannot be ruled out (Figure 4). Given that there are no redundant tracers for this age range, future work interpreting ^{39}Ar in granitic bedrock could employ a numerical modeling approach using particle-tracking to address the confounding factor of subsurface production.

Further, the piston flow age of 10 years for the groundwater located at the Parker well, though the youngest of the groundwaters at the wells considered in this study, was still higher than would be expected from its completion characteristics and proximity (< 800 m) to Sabino Creek. This implies a low average linear velocity of 0.22 m/d, assuming piston flow conditions. Such a value is plausible for the alluvial terrace deposits, which have been shown to be moderately cemented in the Catalina foothills (Mohrbacher, 1984); however, an additional hypothesis is that the tracer concentrations are slightly diluted from older tritium-dead water in the Pantano Formation in which the Parker well is partially completed (Figure 1b). It has been shown that dispersion or exchange of water between the aquifer and surrounding low conductivity units can artificially decrease the concentration of tracers to produce an erroneously older age (Bethke & Johnson, 2002). A mixing model of modern and old groundwater (Table 3) accounted for this exchange process, finding that roughly 1% of the water captured by the well is old. This is further supported by the presence of terrigenous helium in groundwater present in the Parker well, which is roughly 1.8% of the terrigenous helium detected in the Agua Caliente well. Thus, additional environmental tracers such as noble gases are not only complementary to age interpretation but can be crucial for reducing nonuniqueness.

The incongruence between completion characteristics (Figure 1b) and age (PFM age of 22 years) for well B-026b is likely due to proximity to the Rillito river. Previous studies have noted a dominant effect of the ephemeral Rillito River recharge on groundwater ages in the Tucson basin-fill aquifer (Carlson et al., 2011; Eastoe et al., 2004), and it is clear from our study that focused recharge along this stretch of the Rillito is a large enough flux to mute other flow paths to near-stream production wells. Further, modern recharge and more permeable sediment can be found at shallower depths in the Tucson basin-fill aquifer, and so the fact that groundwater collected from well B-026b has a modern age despite having a deep completion and long-screen may instead reflect preferential capture during pumping (Segal et al., 2014; Visser et al., 2013). This

is an important limitation in groundwater age studies sampling from long-screened production wells—if tracer concentrations are permeability-weighted, the interpreted ages will have a modern bias and will not necessarily reflect age distributions for the entire aquifer system. Future work with groundwater age tracers collected from long-screened wells could leverage advances in flow metering (Poulsen et al., 2019) to help reduce this uncertainty.

Finally, while noble gas radioisotope analysis was cost-prohibitive at the time of the study, promising advances such as atom trap trace analysis (ATTA) have decreased the cost and sampling effort barrier for noble gas radioisotopes. ^{81}Kr and ^{85}Kr are now routinely analyzed using ATTA (Jiang et al., 2012), and the technique has been demonstrated for ^{39}Ar (Ritterbusch et al., 2014); however, the cost of analysis remains relatively inaccessible to most routine tracer studies. Our study demonstrates that, in groundwater basins that receive a mix of modern and premodern recharge such as basin-fill aquifers adjacent to mountain blocks, ^{39}Ar is highly informative for age distribution modeling, and more effort should be directed toward making this tracer more widely applied.

5.2. Recharge Elevations

The second hypothesis we posed was that MFR components should be distinguishable by their recharge elevation. If we assume the T_r lapse rate is equal to the T_s lapse rate determined from measuring spring temperatures in the Santa Catalina mountains, the resulting recharge elevations produced results that were counter to the age distributions results (Figure 5). Namely, the wells capturing modern groundwater had lower median T_r 's and thus higher median recharge elevations than the well capturing the oldest groundwater. The groundwater velocities required to satisfy such results are unreasonable in both instances. Hence, we explored the possibility that high rates of surface MFR, sourced from winter runoff, were locally suppressing water table temperatures.

Numerical experiments conducted using VS2DH (Healy & Ronan, 1996; Lappala et al., 1987) simulating a range of fluid and energy transport conceptualizations (Table 2) revealed a strong sensitivity to recharge amount and milder sensitivity to K and temperature of recharge. Regardless of scenario, the modeled T_r lapse rates deviate substantially from the constant T_a and T_s lapse rates (Figure 6). Larger, colder fluxes in the higher elevations produced the coldest water table temperatures, though in all scenarios the modeled water table temperatures were warmer than the T_s and T_a lapse rates. This suggests that the T_s lapse rate determined from springs, which are mainly sourced from snowmelt, do not reflect the temperature of the regional water table in this system. Lower elevations on the mountain block show the largest deviations from the T_s and T_a lapse rates, where recharge fluxes are not high enough or cold enough to suppress the geothermal gradient. The modeled T_r lapse across the mountain block, $-10^\circ\text{C}/\text{km}$ elevation gain, is moderately steeper than both the T_s and T_a lapse rates (-8.5 and $-6^\circ\text{C}/\text{km}$, respectively). Heilweil et al. (2012) found similar behavior in a volcanic island aquifer, where their modeled T_r lapse was $-15^\circ\text{C}/\text{km}$ —twice as steep as their measured T_s lapse rate of $-7.5^\circ\text{C}/\text{km}$. In both cases, the air temperature decrease coupled with an increase in mountain aquifer recharge with increasing elevation likely explains the steeper T_r lapse rates compared to T_s and T_a .

Importantly, discrete fluxes of surface MFR locally suppressed T_r at the basin floor in all scenarios and by up to 10°C compared to T_s (determined by spring temperatures) or T_a . This suppression of NGTs as a result of snowmelt-derived MFR has also been observed in the Central Valley aquifer system, California (Cey et al., 2007; Visser et al., 2018), though the effect on interpreting these locally suppressed NGTs for recharge elevation was not explored. Aside from focused, snowmelt-derived recharge, one other possible explanation for lower NGTs is the presence of paleo-groundwater that recharged under cooler temperatures. Indeed, the presence of Pleistocene groundwater with cooler NGTs (Manning, 2011) and more depleted stable isotopes (Eastoe & Towne, 2018) has been documented in several nearby basin-fill aquifer systems in the US Southwest. Given the predominantly modern ages of shallow groundwater in the Tucson Basin, this explanation is unlikely.

Groundwater at Agua Caliente had the lowest recharge elevation when assuming a constant T_r lapse rate (Figure 5), whereas comparing CE-model results for noble gas T_r to the modeled T_r -lapse rate resulted in a median recharge elevation for groundwater at Agua Caliente of $\sim 2,000$ m, the highest of the six well

locations (Figure 6e). This is because the modeled T_r lapse for the lower mountain block and mountain front is substantially warmer than the constant lapse rates. A lack of springs and wells in the lower zone of the mountain block precludes validation of the modeled T_r lapse behavior for these elevations. Using the mean winter air temperature of the basin floor (13°C) for the specified surface MFR flux, while warmer than the temperature of winter runoff, could result in underestimates of steady-state temperatures in the aquifer. However, our modeling showed that using the mean annual air temperature (19°C) for this flux resulted in consistent overestimates of temperature (Figure 6c, pink). As recharge flux was shown to be the strongest driver of temperature distribution in the basin-fill aquifer (Figure 6a) and given that the applied flux was taken as the lower end of surface MFR estimates from previous modeling and field-based studies (Carlson et al., 2011), these numerical experiments represent conservative estimates of the influence of surface MFR on basin-fill aquifer temperatures.

The revised recharge elevations are in better agreement with the age modeling results (e.g., modern water recharges on the basin floor and old water recharges higher up on the mountain block), and result in age-based velocities that are more realistic. This has important implications for studies using noble gases to investigate MFR, as assuming a constant T_r lapse rate in systems with focused recharge sourced from winter runoff may overestimate recharge elevations. However, our conclusions are based on steady-state numerical experiments and few measurements of recharge and water table temperatures. A major question that remains is how the temporal variability of recharge fluxes and temperature influence the recharge temperature lapse rate in the Tucson basin-fill aquifer. Using a 3-D numerical model capable of simulating the transient temperature and flux of recharge in aquifers receiving surface MFR along with particle-tracking based transit times would further bolster these findings, and provide a key link between recharge temperatures and groundwater age modeling. Such a model was not possible given the data constraints of this study; however, more frequent paired measurements of temperature in streams and wells in both the mountain block and the basin-fill aquifer would improve the reliability of the transport modeling and advance our ability to interpret NGTs for recharge elevations in MFR studies.

5.3. Summary of MFR Components in the Tucson Basin

The combination of groundwater age distributions and noble gas recharge elevations provides a complete, though coarse, picture of both the relative proportions and quantities of MFR components in the Tucson Basin. Age modeling results suggest that diffuse MBR comprises a small proportion (6–7%) of water to two of the four production wells in the basin-fill aquifer, while surface MFR comprises the vast majority of water captured by all four production wells. The relatively low K of the mountain block combined with modest recharge (1–2.5% of annual precipitation) to the mountain aquifer probably favors local flow paths, as opposed to the deep, regional flow paths required for large diffuse MBR amounts (Markovich et al., 2019). Further, the presence of the low K Pantano Formation likely impedes diffuse MBR, perhaps causing these flow paths to refract and enter the basin-fill aquifer system deeper than the zone of capture of the production wells.

The age distribution and noble gas recharge elevations both confirm that groundwater located at Agua Caliente is representative of MBR, and from Equations 6 and 7 we can calculate a rough volumetric flux. From the mean age of 4,300 years and a distance to nearest median recharge elevation of 10 km, we estimate a velocity of 6.4×10^{-3} m/d. Assuming an effective porosity of 0.1, and a cross-sectional area of 200 m (the thickness of weathered granite taken from the Agua Caliente driller's log) by 24 km (length of the Santa Catalina mountain front), we arrive at a flux of 1.1×10^6 m³/year. This value is well within the range estimated from ¹⁴C ages by Kalin (1994) but three to six times smaller than the flux estimated from the electric analog modeling by Anderson (1972).

Assuming the diffuse MBR flux is relatively constant and that other sources of recharge aside from surface MFR are negligible, we can compare our estimated MBR flux to estimates of annual surface MFR fluxes (reviewed by Carlson et al. (2011)). We find that diffuse MBR comprises 2–40% of recharge to the portion of the Tucson basin-fill aquifer along the Santa Catalina mountain front. This estimate does not account for focused MBR, which, given the presence of high-angle normal faulting in the piedmont and the presence of permeable material deposited by streams exiting the mountain block (“shoestring aquifers” described in Mohrbacher (1984)), could allow for preferential flow paths from the mountain block to the basin-fill

aquifer and would thus drive down the fraction of diffuse MBR. Nevertheless, the fractions estimated from age modeling for groundwater at the two C-production wells (6–7%) fall within the lower range of this estimation. Overall, this exercise supports the use of age distributions as an approach for distinguishing and roughly quantifying MFR components captured by basin-fill production wells.

6. Conclusions

Mountain-front recharge is an important component of recharge to basin-fill aquifer systems, particularly in semiarid and arid systems (Markovich et al., 2019; Wilson & Guan, 2004). Distinguishing and quantifying the surface from subsurface components of MFR is necessary for water resource planning and management, particularly as climate change may impact the components in distinct ways (Meixner et al., 2016). This study combined multiple groundwater age tracers along with dissolved noble gas concentrations collected from basin-fill production wells to characterize the full age distributions and mean recharge elevations with the purpose of distinguishing and quantifying MFR components. Energy transport modeling was used to simulate multiple conceptualizations of the system in order to test whether high rates of surface MFR could substantially affect the relationship between water table temperatures and elevation.

Overall, this study found that the groundwater age distributions derived from multiple tracer sources provide valuable information for characterizing the dominant flow system behavior and the source of groundwater captured by the basin-fill production wells. ^3H and ^{39}Ar were the most informative tracers in determining the best-fit age distributions (Table 4), reiterating the importance of using multiple age tracers and highlighting the substantial information gained by ^{39}Ar in filling the age gap between ^3H and ^{14}C . Tracers indicated very old water in a well completed in weathered bedrock located close to the mountain front, and two production wells exhibited age distributions of binary mixing between two components including mainly modern and a small fraction of old water, whereas the remaining wells captured predominantly modern flow paths. This supports our hypothesis that surface MFR and diffuse MBR can be distinguished by age distributions of groundwater captured by production wells.

Noble gases provide information (i.e., the median elevation of recharge) that is complementary to age distributions and can be effective in distinguishing between surface MFR and diffuse MBR components in production wells given the potentially large (1,000s of m) difference in recharge elevations. However, this study found that assuming a constant T_r lapse rate equal to the air temperature or ground surface temperature lapse rate can produce improbable recharge elevations. Numerical experiments of fluid and energy transport modeling suggest that surface MFR recharge can locally suppress water table temperatures in the basin-fill aquifer, which has implications for NGT studies in semiarid, intermontane basin-fill aquifers that receive a major fraction of recharge from snowmelt-derived surface MFR.

Acknowledgments

This work was made possible due to the generous cooperation and support from Dick Thompson of Tucson Water, Trevor Hare of the Watershed Management Group, and the Pima County Department of Parks and Recreation. The first author was supported by an NSF EAR Postdoctoral Fellowship (Award ID 1806383). The U.S.-Mexico Transboundary Aquifer Assessment Act (Public Law 109-448) and Cooperative Agreement Project Between NMSU, NM WRRI, and the U.S. Bureau of Reclamation are gratefully acknowledged for their support and funding of this study. The NSF Santa Catalina mountains and Jemez River Basin Critical Zone Observatory (EAR-1331408) also provided support for this study. The authors declare no real or perceived financial conflicts of interest nor any conflict of interest with respect to the results of this paper.

Data Availability Statement

All chemical, isotopic, and noble gas data generated in this study are included in tables in the main document and supporting information. The TracerLPM workbook, VS2DH, and NETPATH modeling input scripts and outputs are available online at <https://doi.org/10.5281/zenodo.4275040>.

References

- Aeschbach-Hertig, W., Peeters, F., Beyerle, U., & Kipfer, R. (1999). Interpretation of dissolved atmospheric noble gases. *Water Resources Research*, 35(9), 2779–2792. <https://doi.org/10.1029/1999WR900130>
- Aeschbach-Hertig, W., Peeters, F., Beyerle, U., & Kipfer, R. (2000). Palaeotemperature reconstruction from noble gases in ground water taking into account equilibration with entrapped air. *Nature*, 405(6790), 1040–1044. <https://doi.org/10.1038/35016542>
- Aggarwal, P. K., Frohlich, K., Glynn, P. D., Phillips, F. M., Plummer, L. N., Purtschert, R., et al. (2013). Isotope methods for dating old groundwater. Vienna International Atomic Energy Agency. <https://doi.org/10.1080/10406029809379327>
- Ajami, H., Troch, P. A., Maddock, T., Meixner, T., & Eastoe, C. (2011). Quantifying mountain block recharge by means of catchment-scale storage-discharge relationships. *Water Resources Research*, 47, W04504. <https://doi.org/10.1029/2010WR009598>
- Åkesson, M., Suckow, A., Visser, A., Sültenfu, J., Laier, T., Purtschert, R., & Sparrenbom, C. J. (2015). Constraining age distributions of groundwater from public supply wells in diverse hydrogeological settings in Scania, Sweden. *Journal of Hydrology*, 528, 217–229. <https://doi.org/10.1016/j.jhydrol.2015.06.022>
- Althaus, R., Klump, S., Onnis, A., Kipfer, R., Purtschert, R., Stauffer, F., & Kinzelbach, W. (2009). Noble gas tracers for characterisation of flow dynamics and origin of groundwater: A case study in Switzerland. *Journal of Hydrology*, 370(1–4), 64–72. <https://doi.org/10.1016/j.jhydrol.2009.02.053>

- Anderson, T. W. (1972). Electrical-analog analysis of the hydrologic system, Tucson Basin, southeastern Arizona. *U.S. Geological Survey Water-Supply Paper 1939-C*
- Ballentine, C. J., & Hall, C. M. (1999). Determining paleotemperature and other variables by using an error-weighted, nonlinear inversion of noble gas concentrations in water. *Geochimica et Cosmochimica Acta*, 63, 2315–2336. [https://doi.org/10.1016/S0016-7037\(99\)00131-3](https://doi.org/10.1016/S0016-7037(99)00131-3)
- Bartlett, M. G., Chapman, D. S., & Harris, R. N. (2004). Snow and the ground temperature record of climate change. *Journal of Geophysical Research*, 109, F04008. <https://doi.org/10.1029/2004JF000224>
- Belan, R. A. (1972). *Hydrogeology of a portion of the Santa Catalina Mountains* (M.S. thesis, 68 p.). Tucson, AZ: Department of Hydrology and Water Resources, University of Arizona.
- Bethke, C. M., & Johnson, T. M. (2002). Paradox of groundwater age. *Geology*, 30(2), 107–110. [https://doi.org/10.1130/0091-7613\(2002\)030<0107:POGA>2.0.CO;2](https://doi.org/10.1130/0091-7613(2002)030<0107:POGA>2.0.CO;2)
- Bollhöfer, A., Schlosser, C., Schmid, S., Konrad, M., Purtschert, R., & Krais, R. (2019). Half a century of Krypton-85 activity concentration measured in air over Central Europe: Trends and relevance for dating young groundwater. *Journal of Environmental Radioactivity*, 205–206, 7–16. <https://doi.org/10.1016/j.jenvrad.2019.04.014>
- Carlson, M. A., Lohse, K. A., McIntosh, J. C., & McLain, J. E. T. (2011). Impacts of urbanization on groundwater quality and recharge in a semi-arid alluvial basin. *Journal of Hydrology*, 409(1–2), 196–211. <https://doi.org/10.1016/j.jhydrol.2011.08.020>
- Castro, M. C., Stute, M., & Schlosser, P. (2000). Comparison of ^4He ages and ^{14}C ages in simple aquifer systems: Implications for groundwater flow and chronologies. *Applied Geochemistry*, 15, 1137–1167. [https://doi.org/10.1016/S0883-2927\(99\)00113-4](https://doi.org/10.1016/S0883-2927(99)00113-4)
- Cey, B. D., Hudson, G. B., Moran, J. E., & Scanlon, B. R. (2008). Impact of artificial recharge on dissolved noble gases in groundwater in California. *Environmental Science and Technology*, 42, 1017–1023
- Cook, P. G., & Böhlke, J. K. (2000). Determining timescales for groundwater flow and solute transport. In P. G. Cook, & A. L. Herczeg (Eds.), *Environmental tracers in subsurface hydrology* (pp. 379–396). Boston, MA: Kluwer
- Corcho Alvarado, J. A., Purtschert, R., Barbecot, F., Chabault, C., Rueedi, J., Schneider, V., et al. (2007). Constraining the age distribution of highly mixed groundwater using ^{39}Ar : A multiple environmental tracer ($^3\text{H}/^2\text{He}$, ^{85}Kr , ^{39}Ar , and ^{14}C) study in the semiconfined Fontainebleau Sands aquifer (France). *Water Resources Research*, 43, W03427. <https://doi.org/10.1029/2006WR005096>
- Cunningham, E. B., Long, A., Eastoe, C., & Bassett, R. L. (1998). Migration of recharge waters downgradient from the Santa Catalina mountains into the Tucson basin aquifer, Arizona, USA. *Hydrogeology Journal*, 6(1), 94–103. <https://doi.org/10.1007/s100400050136>
- Davidson, E. S. (1973). Geohydrology and water resources of the Tucson Basin, Arizona. *U.S. Geological Survey Water-Supply Paper 1939-E*
- Doyle, J. M., Gleeson, T., Manning, A. H., & Ulrich Mayer, K. (2015). Using noble gas tracers to constrain a groundwater flow model with recharge elevations: A novel approach for mountainous terrain. *Water Resources Research*, 51, 8094–8113. <https://doi.org/10.1002/2015WR017274>
- Dwivedi, R., Meixner, T., McIntosh, J. C., Ferré, P. A. T., Dwivedi, R., Eastoe, C. J., et al. (2019). Hydrologic functioning of the deep critical zone and contributions to streamflow in a high-elevation catchment: Testing of multiple conceptual models. *Hydrological Processes*, 33, 476–494. <https://doi.org/10.1002/hyp.13363>
- Earman, S., Campbell, A. R., Phillips, F. M., & Newman, B. D. (2006). Isotopic exchange between snow and atmospheric water vapor: Estimation of the snowmelt component of groundwater recharge in the southwestern United States. *Journal of Geophysical Research*, 111, D09302. <https://doi.org/10.1029/2005JD006470>
- Eastoe, C. J., & Dettman, D. L. (2016). Isotope amount effects in hydrologic and climate reconstructions of monsoon climates: Implications of some long-term data sets for precipitation. *Chemical Geology*, 430, 78–89. <https://doi.org/10.1016/j.chemgeo.2016.03.022>
- Eastoe, C. J., Gu, A., & Long, A. (2004). The origins, ages and flow paths of groundwater in Tucson Basin: Results of a study of multiple isotope systems. *Water Science and Application*, 9, 217–234
- Eastoe, C. J., & Towne, D. (2018). Regional zonation of groundwater recharge mechanisms in alluvial basins of Arizona: Interpretation of isotope mapping. *Journal of Geochemical Exploration*, 194, 134–145. <https://doi.org/10.1016/j.jgexplo.2018.07.013>
- Eastoe, C. J., Watts, C. J., Ploughe, M., & Wright, W. E. (2012). Future use of tritium in mapping pre-bomb groundwater volumes. *Ground Water*, 50(1), 87–93. <https://doi.org/10.1111/j.1745-6584.2011.00806.x>
- Eastoe, C. J., & Wright, W. E. (2019). Hydrology of mountain blocks in Arizona and New Mexico as revealed by isotopes in groundwater and precipitation. *Geosciences*, 9(461), 22
- Forster, C., & Smith, L. (1989). The influence of groundwater flow on thermal regimes in mountainous terrain: A model study. *Journal of Geophysical Research: Solid Earth*, 94(B7), 9439–9451. <https://doi.org/10.1029/JB094iB07p09439>
- Gardner, P. M., & Heilweil, V. M. (2014). A multiple-tracer approach to understanding regional groundwater flow in the Snake Valley area of the eastern Great Basin, USA. *Applied Geochemistry*, 45, 33–49. <https://doi.org/10.1016/j.apgeochem.2014.02.010>
- Gieskes, J. M., & Rogers, W. C. (1973). Alkalinity determination in interstitial waters of marine sediments. *Journal of Sedimentary Petrology*, 43(1), 272–277. <https://doi.org/10.1306/74d72743-2b21-11d7-8648000102c1865d>
- Harlow, R. C., Burke, E. J., Scott, R. L., Shuttleworth, W. J., Brown, C. M., & Petti, J. R. (2004). Derivation of temperature lapse rates in semi-arid south-eastern Arizona. *Hydrology and Earth System Sciences*, 8(6), 1179–1185
- Healy, R. W. (1990). Simulation of solute transport in variably saturated porous. *U.S. Geological Survey Water-Resources Investigations Report*, 90-4025
- Healy, R. W., & Ronan, A. D. (1996). Documentation of computer program VS2DH for simulation of energy transport in variably saturated porous media—Modification of the U.S. Geological survey's computer program VS2DT. *U.S. Geological Survey Water Resources Investigations Report*, 96-4230, 40
- Heilweil, V. M., Healy, R. W., & Harris, R. N. (2012). Noble gases and coupled heat/fluid flow modeling for evaluating hydrogeologic conditions of volcanic island aquifers. *Journal of Hydrology*, 464–465, 309–327. <https://doi.org/10.1016/j.jhydrol.2012.07.019>
- Hopkins, C. B., McIntosh, J. C., Eastoe, C., Dickinson, J. E., & Meixner, T. (2014). Evaluation of the importance of clay confining units on groundwater flow in alluvial basins using solute and isotope tracers: The case of Middle San Pedro Basin in southeastern Arizona (USA). *Hydrogeology Journal*, 22(4), 829–849. <https://doi.org/10.1007/s10040-013-1090-0>
- Hua, Q., & Barbetti, M. (2004). Review of tropospheric bomb ^{14}C data for carbon cycle modeling and age calibration purposes. *Radiocarbon*, 46(3), 1273–1298. <https://doi.org/10.1017/S0033822200033142>
- Jiang, W., Bailey, K., Lu, Z. T., Mueller, P., O'Connor, T. P., Cheng, C. F., et al. (2012). An atom counter for measuring ^{81}Kr and ^{85}Kr in environmental samples. *Geochimica et Cosmochimica Acta*, 91, 1–6. <https://doi.org/10.1016/j.gca.2012.05.019>
- Jung, M., & Aeschbach, W. (2018). A new software tool for the analysis of noble gas data sets from (ground)water. *Environmental Modelling and Software*, 103, 120–130. <https://doi.org/10.1016/j.envsoft.2018.02.004>
- Jung, M., Wieser, M., von Oehsen, A., & Aeschbach-Hertig, W. (2013). Properties of the closed-system equilibration model for dissolved noble gases in groundwater. *Chemical Geology*, 339, 291–300. <https://doi.org/10.1016/j.chemgeo.2012.08.006>

- Jurgens, B. C., Bohlke, J. K., & Eberts, S. M. (2012). TracerLPM (version 1): An excel(R) workbook for interpreting groundwater age distributions from environmental tracer data. U.S. Geological Survey Techniques and Methods Report 4-F3, (Version 1)
- Kalin, R. M. (1994). *The hydrogeochemical evolution of the groundwater of the Tucson Basin with application to 3-dimensional groundwater flow modelling* (Ph.D. dissertation, 515 p). Tucson, AZ: Department of Hydrology and Water Resources, University of Arizona
- Kipfer, R., Aeschbach-Hertig, W., Peeters, F., & Stute, M. (2008). Noble gases in lakes and ground waters. *Reviews in Mineralogy and Geochemistry*, 47(1), 615–700. <https://doi.org/10.2138/rmg.2002.47.14>
- Kipp, K. L. Jr. (1987). HST3D: A computer code for simulation of heat and solute transport. *U.S. Geological Survey Water-Resources Investigations Report*, 86-4095, 229.
- Lachenbruch, A. H., Sass, J. H., & Morgan, P. (1994). Thermal regime of the southern Basin and range province: 2. Implications of heat flow for regional extension and metamorphic core complexes. *Journal of Geophysical Research*, 99(B11), 22121–22133. <https://doi.org/10.1029/94jb01890>
- Lappala, E. G., Healy, R. W., & Weeks, E. P. (1987). Documentation of computer program VS2D to solve the equations of fluid flow in variably saturated porous media. U.S. Geological Survey Water Resources Investigations Report 83-4099, 193 p.
- Lehmann, B. E., & Loosli, H. H. (1991). Isotopes formed by underground production. In F. J. Pearson, W. Balderer, H. H. Loosli, B. Lehmann, A. Matter, T. Peters, et al. (Eds.), *Applied isotope hydrogeology, a case study in northern Switzerland* (pp. 239–296). Amsterdam: Elsevier.
- Loosli, H. H. (1983). A dating method with ^{39}Ar . *Earth and Planetary Science Letters*, 63(1), 51–62. [https://doi.org/10.1016/0012-821X\(83\)90021-3](https://doi.org/10.1016/0012-821X(83)90021-3)
- Loosli, H. H., Lehmann, B. E., & Balderer, W. (1989). Argon-39, argon-37 and krypton-85 isotopes in Stripa groundwaters. *Geochimica et Cosmochimica Acta*, 53(8), 1825–1829. [https://doi.org/10.1016/0016-7037\(89\)90303-7](https://doi.org/10.1016/0016-7037(89)90303-7)
- Loosli, H. H., Lehmann, B. E., & Smethie, W. M. Jr. (2000). Noble gas radioisotopes: ^{37}Ar , ^{85}Kr , ^{39}Ar , ^{81}Kr . In P. G. Cook, & A. L. Herczeg (Eds.), *Environmental tracers in subsurface hydrology* (pp. 379–396). Boston, MA: Kluwer.
- Loosli, H. H., & Purtschert, R. (2005). Rare gases. In P. K. Aggarwal, J. R. Gat, & K. F. O. Froehlich (Eds.), *Isotopes in the water cycle: Past, present, and future of a developing science* (pp. 91–95). Vienna: IAEA.
- Maloszewski, P., & Zuber, A. (1996). Lumped parameter models for the interpretation of environmental tracer data. In international atomic energy agency. *Manual on mathematical models in isotope hydrogeology, TECDOC-910* (pp. 9–58). Vienna: International Atomic Energy Agency Publishing Section.
- Manning, A. H. (2011). Mountain-block recharge, present and past, in the eastern Española Basin, New Mexico, USA. *Hydrogeology Journal*, 19(2), 379–397. <https://doi.org/10.1007/s10040-010-0696-8>
- Manning, A. H., & Solomon, D. K. (2003). Using noble gases to investigate mountain-front recharge. *Journal of Hydrology*, 275(3–4), 194–207. [https://doi.org/10.1016/S0022-1694\(03\)00043-X](https://doi.org/10.1016/S0022-1694(03)00043-X)
- Manning, A. H., & Solomon, D. K. (2004). Constraining mountain-block recharge to the eastern Salt Lake Valley, Utah with dissolved noble gas and tritium data. *Groundwater Recharge in A Desert Environment: The Southwestern United States*, 9, 139–158.
- Manning, A. H., & Solomon, D. K. (2005). An integrated environmental tracer approach to characterizing groundwater circulation in a mountain block. *Water Resources Research*, 41, W12412. <https://doi.org/10.1029/2005WR004178>
- Markovich, K. H., Manning, A. H., Condon, L. E., & McIntosh, J. C. (2019). Mountain-block recharge: A review of current understanding. *Water Resources Research*, 55, 8278–8304. <https://doi.org/10.1029/2019wr025676>
- Mason, D., & Hipke, W. (2013). Regional groundwater flow model of the Tucson active management area, Arizona. *Arizona Department of Water Resources*.
- McCallum, J. L., Dogramaci, S., Cook, P. G., Banks, E., Purtschert, R., Irvine, M., et al. (2018). Stochastic correction of carbon-14 activities: A Bayesian approach with argon-39 validation. *Journal of Hydrology*, 566, 396–405. <https://doi.org/10.1016/j.jhydrol.2018.08.047>
- Meixner, T., Manning, A. H., Stonestrom, D. A., Allen, D. M., Ajami, H., Blasch, K. W., et al. (2016). Implications of projected climate change for groundwater recharge in the western United States. *Journal of Hydrology*, 534, 124–138. <https://doi.org/10.1016/j.jhydrol.2015.12.027>
- Merz, A. (1985). *Mountain-front recharge from the Santa Rita mountains to the Tucson basin* (M.S. thesis, 122 p.). Tucson, AZ: Department of Hydrology and Water Resources, University of Arizona.
- Mohrbacher, C. J. (1984). *Mountain-front recharge to the Tucson basin from the Santa Catalina mountains, Arizona* (M.S. thesis, 229 p.). Tucson, AZ: Department of Hydrology and Water Resources, University of Arizona.
- Morgenstern, U., Stewart, M. K., & Stenger, R. (2010). Dating of streamwater using tritium in a post nuclear bomb pulse world: Continuous variation of mean transit time with streamflow. *Hydrology and Earth System Sciences*, 14(11), 2289–2301. <https://doi.org/10.5194/hess-14-2289-2010>
- Olson, M. C. (1982). *Mountain-front recharge to the Tucson Basin from Tanque Verde Canyon, Arizona* (M.S. thesis, 124 p.). Tucson, AZ: Department of Hydrology and Water Resources, University of Arizona.
- Peters, E., Visser, A., Esser, B. K., & Moran, J. E. (2018). Tracers reveal recharge elevations, groundwater flow paths and travel times on Mount Shasta, California. *Water*, 10(2), 97. <https://doi.org/10.3390/w10020097>
- Plummer, L. N., Prestemon, E. C., & Parkhurst, D. L. (1994). An interactive code (NETPATH) for modeling net geochemical reactions along a flow path, version 2.0. U.S. Geological Survey Water-Resources Investigations Report, 94-4169, 135.
- Poulsen, D. L., Cook, P. G., Simmons, C. T., Solomon, D. K., & Dogramaci, S. (2019). Depth-resolved groundwater chemistry by longitudinal sampling of ambient and pumped flows within long-screened and open borehole wells. *Water Resources Research*, 55, 9417–9435. <https://doi.org/10.1029/2019WR025713>
- Reimer, P. J., Baillie, M. G. L., Bard, E., Bayliss, A., Beck, J. W., Blackwell, P. G., et al. (2009). IntCal09 and Marine09 radiocarbon age calibration curves, 0–50,000 years cal bp. *Radiocarbon*, 51(4), 1111–1150. <https://doi.org/10.1017/S0033822200034202>
- Riedmann, R. A., & Purtschert, R. (2016). Separation of argon from environmental samples for Ar-37 and Ar-39 analyses. *Separation and Purification Technology*, 170, 217–223. <https://doi.org/10.1016/j.seppur.2016.06.017>
- Ritterbusch, F., Ebser, S., Welte, J., Reichel, T., Kersting, A., Purtschert, R., et al. (2014). Groundwater dating with atom trap trace analysis of ^{39}Ar . *Geophysical Research Letters*, 41, 6758–6764. <https://doi.org/10.1002/2014GL061120>
- Sass, J. H., Lachenbruch, A. H., Galanis, S. P. Jr., Morgan, P., Priest, S. S., Moses, T. H., & (1994). Thermal regime of the southern Basin and range province: 1. Heat flow data from Arizona and the Mojave Desert and Nevada. *Journal of Geophysical Research*, 99(B11), 22093–22119. <https://doi.org/10.1029/94JB01891>
- Schlosser, P., Stute, M., Dörr, H., Sonntag, C., & Münnich, K. O. (1988). Tritium/ ^3He dating of shallow groundwater. *Earth and Planetary Science Letters*, 89(3–4), 353–362. [https://doi.org/10.1016/0012-821X\(88\)90122-7](https://doi.org/10.1016/0012-821X(88)90122-7)

- Schlosser, P., Stute, M., Sonntag, C., & Münnich, K. O. (1989). Tritogenic ^3He in shallow groundwater. *Earth and Planetary Science Letters*, 94, 246–256.
- Segal, D. C., Moran, J. E., Visser, A., Singleton, M. J., & Esser, B. K. (2014). Seasonal variation of high elevation groundwater recharge as indicator of climate response. *Journal of Hydrology*, 519, 3129–3141.
- Sing, B., & Chen, J. (2014). Nuclear data sheets for A=85. *Nuclear Data Sheets*, 166, 1–162. <https://doi.org/10.1016/j.nds.2014.01.001>
- Solomon, D. K. (2000). ^4He in Groundwater. P. G. Cook & A. L. Herczeg (Eds.). *Environmental tracers in subsurface hydrology*. (pp. 425–439). Boston, MA: Springer. https://doi.org/10.1007/978-1-4615-4557-6_14
- Solomon, D. K., & Cook, P. G. (2000). ^3H and ^3He . In P. G. Cook, & A. L. Herczeg (Eds.), *Environmental tracers in subsurface hydrology* (pp. 397–424). Boston, MA: Kluwer.
- Šrámek, O., Stevens, L., McDonough, W. F., Mukhopadhyay, S., & Peterson, R. J. (2017). Subterranean production of neutrons, ^{39}Ar and ^{21}Ne : Rates and uncertainties. *Geochimica et Cosmochimica Acta*, 196, 370–387. <https://doi.org/10.1016/j.gca.2016.09.040>
- Taylor, R. G., Scanlon, B. R., Doll, P., Rodell, M., van Beek, R., Wada, Y., et al. (2013). Ground water and climate change. *Nature Climate Change*, 3, 322–329. <https://doi.org/10.1038/NCLIMATE1744>
- Visser, A., Broers, H. P., Purtschert, R., Sültenfuß, J., & De Jonge, M. (2013). Groundwater age distributions at a public drinking water supply well field derived from multiple age tracers (^{85}Kr , $^3\text{H}/^3\text{He}$, and ^{39}Ar). *Water Resources Research*, 49, 7778–7796. <https://doi.org/10.1002/2013WR014012>
- Visser, A., Moran, J. E., Singleton, M. J., & Esser, B. K. (2018). Importance of river water recharge to the San Joaquin Valley groundwater system. *Hydrological Processes*, 32(9), 1202–1213.
- Vogel, J. C. (1967). Investigation of groundwater flow with radiocarbon. In *Isotopes in hydrology* (pp. 355–369). Vienna: IAEA.
- Welch, L. A., & Allen, D. M. (2014). Hydraulic conductivity characteristics in mountains and implications for conceptualizing bedrock groundwater flow. *Hydrogeology Journal*, 22(5), 1003–10026. <https://doi.org/10.1007/s10040-014-1121-5>
- Wilson, J. L., & Guan, H. (2004). Mountain-block hydrology and mountain-front recharge. In F. Phillips, J. Hogan, & B. Scanlon (Eds.), *Groundwater recharge in a desert environment, the southwestern United States*. Washington, DC: American Geophysical Union. <https://doi.org/10.1029/009WSA08>
- Yokochi, R. (2016). Recent developments on field gas extraction and sample preparation methods for radiokrypton dating of groundwater. *Journal of Hydrology*, 540, 368–378. <https://doi.org/10.1016/j.jhydrol.2016.06.020>
- Yokochi, R., Sturchio, N. C., & Purtschert, R. (2012). Determination of crustal fluid residence times using nucleogenic ^{39}Ar . *Geochimica et Cosmochimica Acta*, 88, 19–26.

References From the Supporting Information

- Kalin, R. M. (2000). Radiocarbon dating of groundwater systems. In P. G. Cook, & A. L. Herczeg (Eds.), *Environmental tracers in subsurface hydrology* (pp. 111–144). Boston, MA: Springer. https://doi.org/10.1007/978-1-4615-4557-6_4
- Ketcham, R. A. (1996). Distribution of heat-producing elements in the upper and middle crust of southern and west central Arizona: Evidence from the core complexes. *Journal of Geophysical Research*, 101(B6), 13611–13632. <http://dx.doi.org/10.1029/96JB00664>
- McPherson, G. R., Boutton, T. W., & Midwood, A. J. (1993). Stable carbon isotope analysis of soil organic matter illustrates vegetation change at the grassland/woodland boundary in southeastern Arizona, USA. *Oecologia*, 93, 95–101. <https://doi.org/10.1007/BF00321197>
- Mook, W. G., Bommerson, J. C., & Staverman, W. H. (1974). Carbon isotope fractionation between dissolved bicarbonate and gaseous carbon dioxide. *Earth and Planetary Science Letters*, 22(2), 169–176. [https://doi.org/10.1016/0012-821X\(74\)90078-8](https://doi.org/10.1016/0012-821X(74)90078-8)
- Robertson, F. N. (1992). Radiocarbon dating of groundwater in a confined aquifer in southeast Arizona. *Radiocarbon*, 34(3), 664–676.
- Saar, M. O., Castro, M. C., Hall, C. M., Manga, M., & Rose, T. P. (2005). Quantifying magmatic, crustal, and atmospheric helium contributions to volcanic aquifers using all stable noble gases: Implications for magmatism and groundwater flow. *Geochemistry, Geophysics, Geosystems*, 6, Q03008. <https://doi.org/10.1029/2004GC000828>